



p-type a-SiO_x:H as a Hole Transport Layer in p-i-n Perovskite Solar Cells

- John Ian Pold

7th March - 31st August 2017

Supervisors:

UTRECHT UNIVERSITY
dr. Wilfried van Sark

SOLLIANCE ECN, EINDHOVEN
dr. Sjoerd Veenstra
dr. Dong Zhang

ABSTRACT

P-type a-SiO_x:H (p-a-SiO_x:H) was investigated as a hole transport layer (HTL) in perovskite solar cells (PSCs). First p-a-SiO_x:H layers were fabricated and characterised then full cells were fabricated and their IV-characteristics studied. It was discovered that a large barrier is present preventing efficient extraction of the holes from the perovskite into the HTL, resulting in the cells possessing very low short-circuit currents, fill factors and efficiencies. Different combinations of materials, and a UV + ozone treatment, were tested to investigate the cause of this barrier. It is thought that a number of factors could be responsible, namely, poor wetting of the perovskite solution on p-a-SiO_x:H leading to poor microscopic contact between the two materials, non-optimal valence band alignment of the perovskite and p-a-SiO_x:H, and/or low conductivity of p-a-SiO_x:H. At the current status and without further investigation, it cannot be concluded whether p-a-SiO_x:H can be used as a HTL in perovskite solar cells.

TABLE OF CONTENTS

Abstract	I
List of Abbreviations	IV
1. Introduction.....	5
2. Theory	9
Basic Semiconductor Physics.....	9
Atomic Structure & Band Theory.....	9
Density of States & Fermi-Dirac Distribution	9
Doping	10
pn-Junction	11
Solar Cell: Absorption, Generation, Separation, Collection	12
Perovskite Solar cell	13
3. Research Proposal.....	16
4. Fabrication & Characterisation Techniques.....	17
RF Magnetron Sputter Deposition	17
Plasma Enhanced Chemical Vapour Deposition (PECVD)	17
Spin-Coating	18
Thermal Evaporation	18
Kelvin Probe	19
Dark Conductivity & Activation energy	20
Hall Probe.....	20
4-Point Probe	20
IV.....	21
Contact angle measurements.....	22
5. Experimental Section.....	23
Fabrication of Solar Cells	23
6. Results & Discussion	27
Characterisation of p-a-SiO _x :H.....	27
Reflectance/Transmittance	27
Kelvin Probe	28
Activation Energy & Dark Conductivity	31
Solar Cells.....	33
p-a-SiO _x :H (10 & 20 nm) as HTL.....	33
p-a-Si:H (3, 6, 10 nm) as HTL	35
Wetting Issue – Contact Angle Measurements	36
UV/Ozone treatment of p-a-SiO _x :H before perovskite deposition	41
p-a-SiO _x :H & Cu:NiO _x as HTL.....	42

7. Conclusion & Future Work	44
8. Acknowledgements	46
9. Appendices.....	47
Appendix A – Work functions of various materials measured using the Kelvin Probe	47
Appendix B – Properties of ITO.....	47
10. References	48

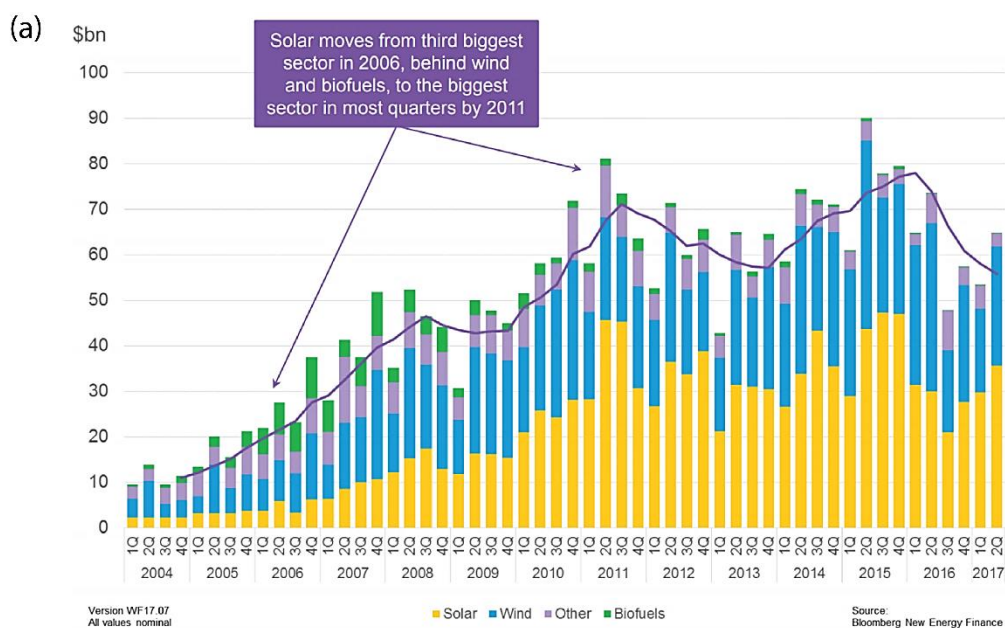
LIST OF ABBREVIATIONS

BIPV	Building integrated photovoltaics
CB	Conduction band
CPD	Contact potential difference
EA	Acceptor energy level
EC	Energy of conduction band edge
ED	Donor energy level
EF	Fermi level
E _g	Band gap
ETL	Electron transport layer
EV	Energy of valence band edge
EVAC	Energy level of vacuum
FF	Fill factor
HOMO	Highest occupied molecular orbital
HTL	Hole transport layer
I _{sc}	Short-circuit current
ITO	Indium tin oxide
KP	Kelvin probe
LUMO	Lowest unoccupied molecular orbital
MPP	Maximum Power Point
<i>n</i>	Electron concentration
<i>p</i>	Hole concentration
P3HT	Poly(3-hexylthiophene-2,5-diyl)
p-a-Si:H	p-type hydrogenated amorphous silicon
p-a-SiO _x :H	p-type hydrogenated amorphous silicon oxide
PECVD	Plasma-enhanced chemical vapour deposition
PEDOT:PSS	poly(3,4-ethylenedioxythiophene)
PTAA	Poly[bis(4-phenyl)(2,4,6-trimethylphenyl)amine]
RF	Radio-frequency
SCR	Space charge region
Spiro-MeOTAD	2,2',7,7'-Tetrakis-(N,N-di-4-methoxyphenylamino)-9,9'-spirobifluorene.
TCO	Transparent conductive oxide
VB	Valence band
VOC	Open-circuit voltage
WF	Work function

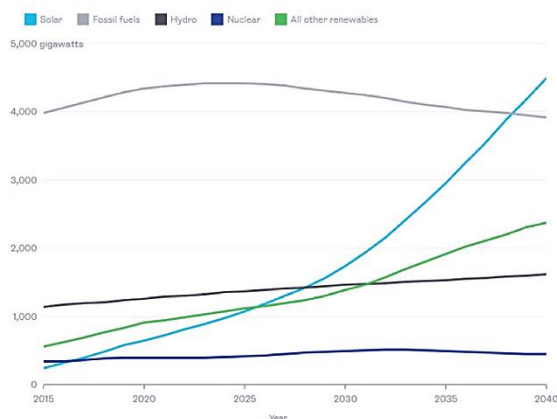
1. INTRODUCTION

The clean energy revolution is here and is happening now. The waking up to the reality of the current and future effects of anthropogenic climate change has led to a boom in renewable energy investment and installation (Figure 1a). It is not only climate change effects such as rising sea levels and extreme weather which can be tackled by renewable energy however, the move away from polluting energy sources such as fossil fuels will also improve air quality, particularly in countries such as China.

Solar energy in particular is coming to the forefront of renewable energy sources and will become the dominant renewable energy source in the not-too-distant future. Already this year solar is predicted to surpass nuclear generation, whilst it will overtake wind in 2022, gas in 2031 and coal in 2032 (Figure 1b). This will make solar, in 2032, the largest single source of capacity globally. In 2039, solar capacity will exceed all fossil fuel capacity (Figure 1c).^[1]



(b) Cumulative installed power generation capacity by technology



(c) Solar Beats Coal in 2032 ...
Cumulative installed power generation capacity by technology

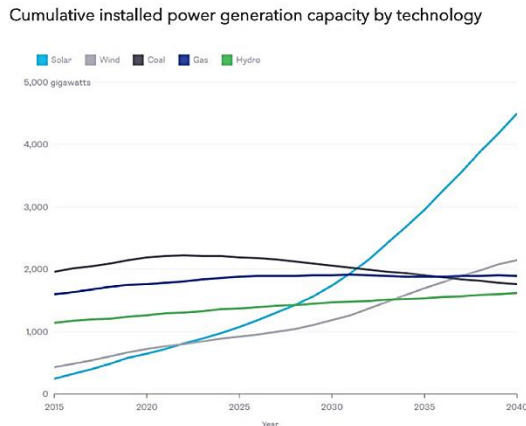


Figure 1. (a) Investment in renewable energy from 2004 to 2017, broken down by technology type. (b) Cumulative installed power generation by technology. (c) Cumulative installed power generation by technology.^[1]

A key reason for the uptake of solar energy has been the consistent decline in manufacturing costs which in turn equates to falling prices of solar panels for individual consumers, utility companies, and governments. The cost of manufacturing falls as the cumulative installed capacity increases - in what is known as a learning curve - due to the ability of manufacturers to learn from previous experiences on how to make their processes more efficient, research and development yields cheaper materials and more efficient solar cells and economies of scale come into play (Figure 2).

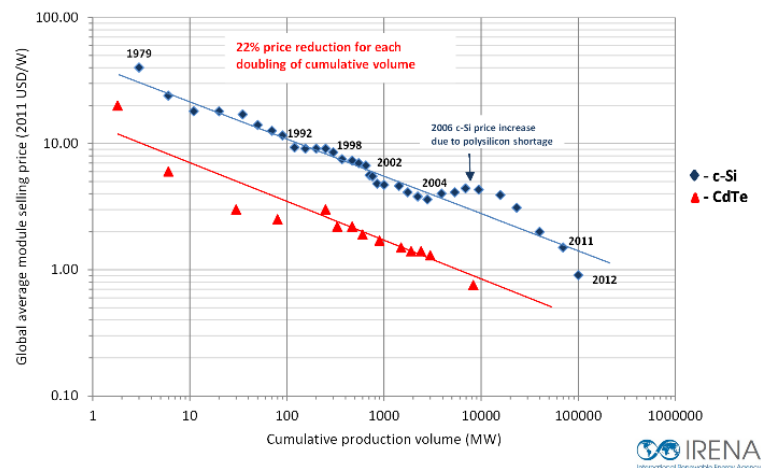


Figure 2. Module cost learning curve for crystalline silicon and thin-film solar cells. [2]

By far the most dominant material solar cells are made out of is silicon (c-Si), making up around 90% of all solar panels in the world. [3] Silicon, however, is actually quite inefficient at absorbing light due to it possessing an indirect band-gap, resulting in the need to use a thick layer of it in the solar cell (140-200 μm). Additionally, in order to achieve an efficient solar cell, a requirement of the silicon wafer is for it to be extremely pure (on the order of 99.999%) and defect free. The silicon wafers are generally produced by the Czochralski method which involves slowly pulling a small crystal of silicon out of a pot of molten silicon to form large cylindrical ingots, which are then cut into thin wafers and further processing steps applied until the silicon is of the certain specifications desired. The whole process is very energy intensive and a lot of material goes to waste. On top of that, because the silicon layer needs to be very thick the solar panels are brittle and heavy. Its brittleness prevents its use in applications where the solar panels may endure mechanical stresses, e.g. in automobiles, or in any non-planar design application, e.g. around curves, preventing many building-integrated PV (BIPV) applications. The combination of all these factors leads to a relatively expensive manufacturing process for silicon solar cells and limits their application in anything other than the standard rooftop of utility solar farm scenario.

As a response to these issues, a second generation of solar cells - the so-called thin-film solar cells - emerged as an alternative to silicon, utilising materials with a direct band-gap which made them much more efficient at absorbing light and so much less material could be used. CdTe and CIGS (copper gallium indium selenium) are the two thin-film technologies currently being industrially produced, though for a few years there was also amorphous silicon solar cells. CdTe, which has the biggest market share of all thin-film technologies, and CIGS both have record efficiencies of over 20% as well as good long-term module stability comparative to silicon solar cells. [4] In addition, the much-reduced thickness - hundreds of nanometres rather than hundreds of micrometres - allows them a certain flexibility, opening up BIPV and other possibilities. CdTe and CIGS solar cells do, however, have their own limitations such as toxicity of certain elements, e.g. Cd, and/or abundance of certain elements, e.g. In, that comprise the cells. At the relatively low market share (~10%) and cumulative volume of installed thin-film PV worldwide, there is not currently a pressing issue with regards to material scarcity, however, in the coming decades with the drive for a 50% share in total energy production by PV by 2050, [4] this could become a serious problem. This is not to say silicon solar cells will not face similar issues, there could also be scarcity challenges with regards to silver used in the contacts.

Third generation solar cell technologies show promise to be able to address material scarcity issues, further lower material costs and also improve the efficiency of existing solar cell technologies. In this third-generation category contains ideas such as multi-junction solar cells (to harvest more of the solar spectrum), using nanomaterials such as quantum dots (either as solar cells themselves or in advanced light management functions, e.g. light trapping or shifting of the spectrum), or using different materials altogether, e.g. dye-sensitized solar cells, organic solar cells, and perovskite solar cells.

Perovskite Solar Cells

Perovskite is the crystal structure of the mineral Perovskite (CaTiO_3), but the name is given to any material which can be described by the generic formula ABX_3 , where A and B are cations and X an anion (Figure 3). Perovskites can exhibit many interesting properties such as superconductivity [5], giant magnetoresistance [6], and catalytic properties [7], however, it is their photovoltaic properties which have really brought them into the spotlight in recent years. [8]

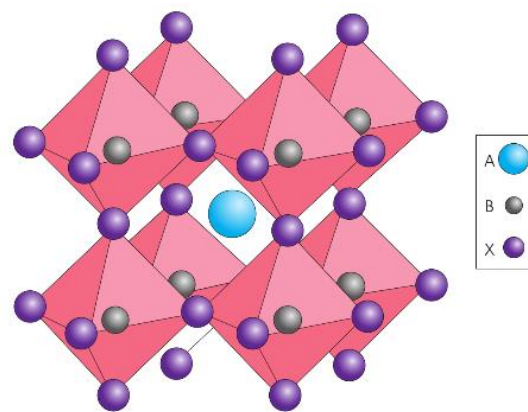


Figure 3. The perovskite crystal structure. [8]

As can be seen from Figure 4, record perovskite solar cell efficiencies have increased very rapidly in a matter of only a few years to reach efficiencies comparable to c-Si and other thin-film solar cells. A major selling point about perovskites is the fact that they are made of cheap, Earth abundant materials. As mentioned previously, material scarcity will become an issue with other solar cell technologies and so for the next generation of solar cells it is important – for the technology to be a viable addition/replacement of current solar cell technologies – to have abundant materials to be able to mass produce the solar cell. As perovskites possess a direct band gap, only a very thin layer of perovskite is required for efficient light harvesting. Cheap initial material costs combined with the need to only use a small amount of it in a solar cell, offers a substantial potential cost-saving compared to existing technologies. On top of that, many perovskites can be solution processed – a much cheaper alternative than vapour deposition processes requiring large vacuum systems. Furthermore, the equipment necessary for solution processing, e.g. slot-die coating, is up-scalable to industrial size and can handle roll-to-roll processes, enabling hundred/thousands or metres of solar cell to be printed on a production line in one run.

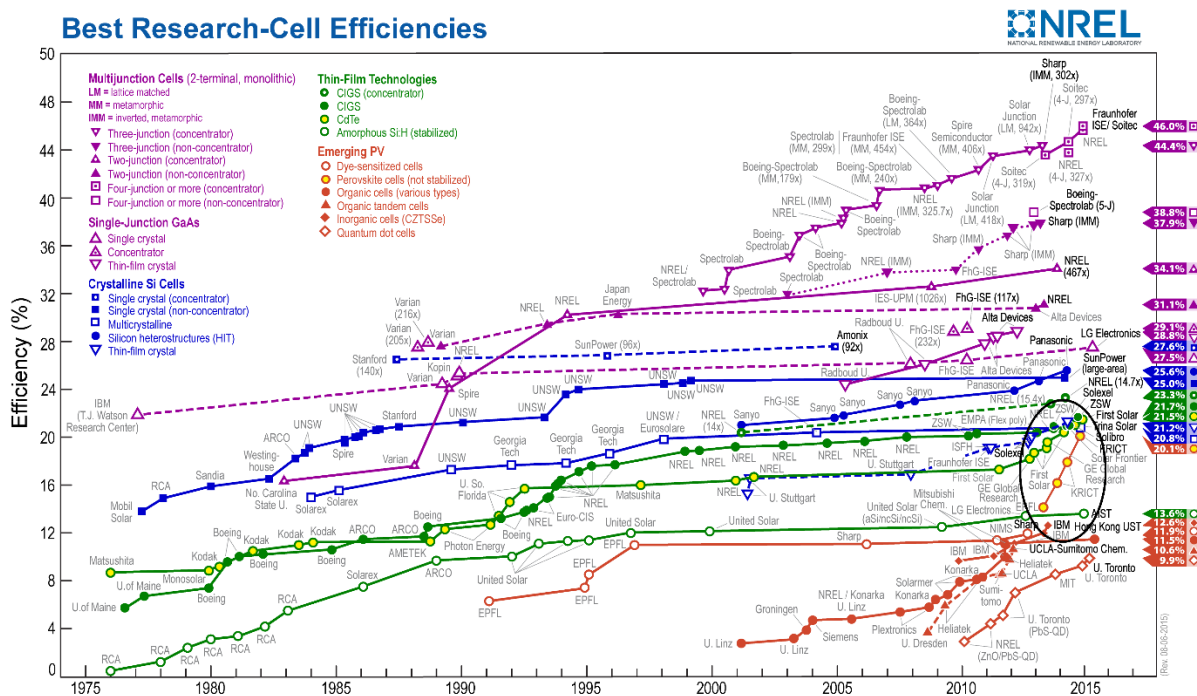


Figure 4. Record research solar cell efficiencies. Circled in black is the efficiencies of perovskite solar cells.^[9]

On the face of it perovskites appear to be the ideal solar cell material and perfect candidate for the next step in the PV evolution. However, there are still sizable obstacles to be overcome before commercialisation and mass production can begin, namely stability. Currently, c-Si solar cells have a standard warranty of 25 years and are expected after this time to still maintain no less than 80% of their initial power output.^[10] Perovskite solar cells on the other hand have not been demonstrated to be able to remain stable for any comparative length of time. Early perovskite solar cells would degrade in hours or days and more recently they have been showing stability for months, even for over a year^[11], however without further improvement their operational stability will continue to fail market requirements as large-scale investments to manufacture perovskite solar cells would be too financially risky.

Perovskite degradation can be due to a wide variety of factors which can vary in significance depending on the exact materials used and architecture of the solar cells. In general, however, these factors can be water and moisture, ultraviolet light and thermal stress^[7,8]. The perovskites, $\text{CH}_3\text{NH}_3\text{X}$ and $\text{CH}(\text{NH}_2)_2\text{X}$ (where X is a halide), for instance, have been shown to undergo hydrolysis by water back to their original precursors PbX_2 and $\text{X}_{1/4}$, a process that is dramatically accelerated by heat, UV light, and electric field.^[12] It is not only the perovskite itself which can undergo degradation however, other parts of the solar cell may also experience this, e.g. the hole transport layer (HTL).^[12]

Perovskite solar cells often employ organic polymers as the HTL, such as PEDOT:PSS^[13], spiro-OMeTAD^[14], P3HT^[15], and PTAA^[16]. Stability issues aside, they are also very expensive, have low hole mobility and cannot withstand high temperatures.^[17] The expense limits the potential for commercialisation whereas the low hole mobility limits the efficiency of the solar cell, and the inability to withstand high temperatures can create problems in the fabrication process of the solar cell due to the possibility of high temperatures being required in subsequent processing steps. As a result, there is a drive to find alternative inorganic HTLs which can address these issues such as NiO^[11], CuI,^[17] and CuSCN^[18]. In this report an alternative material, (boron doped) p-type hydrogenated amorphous silicon oxide (p-a-SiOx:H), is investigated to see whether it can be used as a HTL in perovskite solar cells.

2. THEORY

BASIC SEMICONDUCTOR PHYSICS

ATOMIC STRUCTURE & BAND THEORY

To understand how solar cells operate, one must first understand how semiconductors behave. Silicon (Si) is taken as an example material as it is by far the most common type of material used in solar cells and can illustrate well how the atomic structure leads to the way it bonds and the bands that arise because of it. Si has the electron configuration $[\text{Ne}]3s^23p^2$, meaning the core electrons take the same configuration as neon and the 3s and 3p electrons are its valence electrons. In Si the valence electrons sp^3 hybridise to give atomic orbitals possessing tetrahedral geometry relative to each other. To establish a bond between Si atoms, the atomic orbitals first approach each other and then begin to overlap as they get close. Due to the Pauli exclusion principle, in which no two identical electrons can occupy the same quantum state simultaneously, the sp^3 orbitals are split into two levels - a bonding (highest occupied molecular orbital (HOMO)) and anti-bonding (lowest unoccupied molecular orbital (LUMO)) energy level. As the HOMO is lower in energy than both the LUMO and the energy levels of the original two sp^3 levels, the electrons prefer to fill this state and so form a bond, with one electron with spin up and the other spin down (Figure 5, left). An important aspect about bonding and anti-bonding orbitals is that the energy of the levels depends on the distance between the atoms. The closer the atoms are together the greater the energy splitting and vice versa.

In solar cells Si does not exist as two isolated bonded atoms, instead it is made up of billions and billions of atoms bonding to each other to form an extended periodic lattice. For each of these bonds the energy levels split to form a HOMO and a LUMO, however, because there is a variation of the distances between Si atoms (due to atoms vibrating), there is some difference in the energy of the HOMO and LUMO in each bond. The huge number of energy levels of slightly different energy leads effectively to a continuum of allowed energy levels, called bands. The combination of HOMOs form the valence band (VB) and the combination of LUMOs form the conduction band (CB). The VB edge, *i.e.* the highest attainable VB energy, is denoted E_V and the CB edge, *i.e.* the lowest attainable CB energy, is denoted E_C . The energy difference between E_V and E_C , *i.e.* $E_C - E_V$, is called the band gap (E_g) (Figure 5, right). For crystalline Si the band gap at 300K is 1.12 eV.

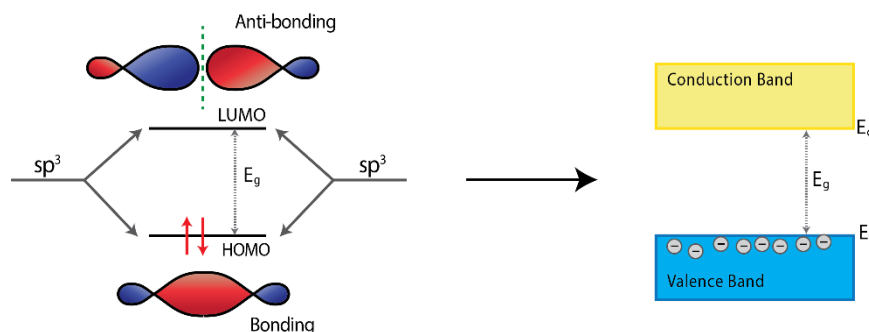


Figure 5. sp^3 hybridised atomic orbitals come together to form a bonding and anti-bonding orbital. In a crystal the energy of each of these orbitals is slightly different and for a continuum of allowed energies, known as bands.

DENSITY OF STATES & FERMI-DIRAC DISTRIBUTION

There are no allowed energy levels in the E_g for the electrons to reside in and so the electrons must either occupy the VB or CB. As the VB is lower in energy than the CB, most electrons will populate the CB, however, if energy is provided to the electron which is greater than or equal to E_g , the electron may be promoted from the VB to CB, leaving a hole behind in the VB. This energy could be in the form of thermal energy (heat) or by absorption of a photon.

The density of states (DOS) function, $g(E)$, describes the number of allowed states that an electron can reside in per unit volume and energy. This can be written for both the CB and VB:

$$g_C(E) = 4\pi \left(\frac{2m_n^*}{h^2} \right)^{\frac{3}{2}} \sqrt{E - E_C} \quad g_V(E) = 4\pi \left(\frac{2m_p^*}{h^2} \right)^{\frac{3}{2}} \sqrt{E_V - E}$$

where m_n^* and m_p^* are the effective masses of electrons and holes, respectively.

The Fermi-Dirac distribution function, $f(E)$, describes the ratio of states filled with an electron to allowed states at a given energy E , and is given by the equation:

$$f(E) = \frac{1}{1 + \exp\left(\frac{E - E_F}{k_B T}\right)}$$

where k_B is the Boltzmann constant and E_F is the Fermi energy (also called Fermi level). The Fermi level is the electrochemical potential of the electrons in a material and represents the averaged energy of electrons in the material. As can be seen from $k_B T$ in the equation, the distribution of electrons depends on thermal energy. At 0 K the denominator equals one and all of the electrons can be found below E_F . As the temperature increases, electrons could populate higher energy levels above E_F , however, they are still bound by the restriction that they cannot reside in the band gap and so any states predicted to be statistically accessible in the band gap will be unoccupied.

The DOS and Fermi-Dirac distribution can be combined to calculate the concentration of electrons, n , in the CB and concentration of holes, p , in the VB, by multiplying the two functions together and integrating across the whole energy band:

$$n(E) = g_C(E)f(E) \quad n = \int_{E_C}^{E_{top}} n(E) dE \quad (1)$$

$$p(E) = g_V(E)[1 - f(E)] \quad p = \int_{E_{bottom}}^{E_V} p(E) dE$$

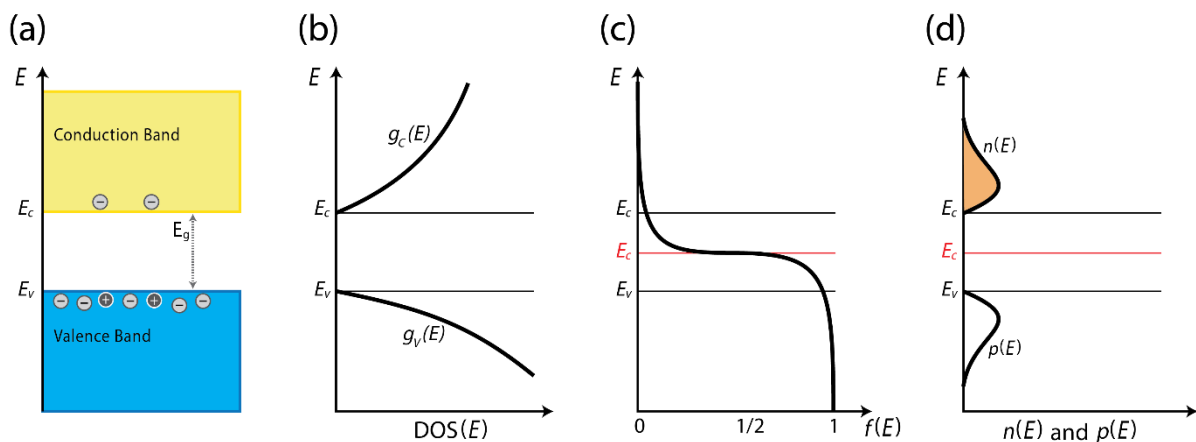


Figure 6. (a) Band energy levels. (b) Density of states. (c) Fermi-Dirac distribution. (d) Electron and hole concentrations as a function of energy.

DOPING

Semiconductors can be doped with atoms of other elements to increase the concentration of electrons or holes (thus increasing the conductivity), depending on whether the dopant has more or less electrons than the material. As Si has four valence electrons it can form four bonds to other

Si atoms. A dopant which replaces a Si atom will itself only be able to form four bonds to neighbouring Si atoms, as a rearrangement of the crystal structure to accommodate less or more bonds is energetically unfavourable. If the dopant has more valence electrons, e.g. phosphorus (P) with five valence electrons, the P atom will form four bonds to Si atoms and the remaining valence electron will remain loosely bound to the P. As it is loosely bound, absorption of even a relatively small amount of thermal energy (which is present in the material at room temperature) can cause it to be ionized, thus increasing the concentration of electrons in the material. Vice versa, if a dopant has less valency electrons, e.g. boron (B) with three valence electrons, the B atom will only be able form three bonds to neighbouring Si atoms but can “accept” an electron from a nearby Si-Si bond. The removal of an electron from the Si lattice creates a hole, thus increasing the hole concentration, which can then subsequently move around.

Introducing dopants into a semiconductor creates allowed energy levels in the forbidden band gap. For an n-type (electron donating) dopant, these donor energy levels (E_D) are produced just below the CB edge (Figure 7b). The electron is localised in the vicinity of the donor but as the energy gap between E_D and E_C is small, it can be easily ionised. Similarly, p-type dopants create allowed energy levels (E_A) just above the VB edge which allow for electrons to be easily promoted from the VB, leaving a hole behind. (Figure 7c).

Doping influences the position of the Fermi level. An increased donor concentration increases the electron concentration and as these electrons are positioned higher in energy near to the CB, the Fermi level is raised towards the CB (Figure 7b). P-doping increases the hole concentration and thus decreases the electron concentration (due to recombination), thus the Fermi level is lowered towards the VB (Figure 7c).

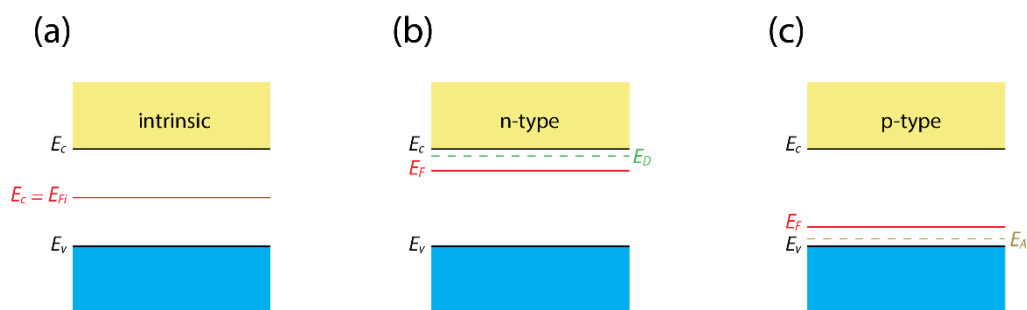


Figure 7. (a) Intrinsic semiconductor. (b) n-type semiconductor. (c) p-type semiconductor.

PN-JUNCTION

Figure 8a schematically shows isolated pieces of an n-type and p-type material and their respective band diagrams. As mentioned in the previous section, in n-type materials the donor electrons are easily promoted from the donor energy levels into the CB, leaving behind a positively charged ion. In a p-type material, electrons are easily excited to the acceptor energy levels thus negatively charging the acceptor atom and creating holes in the VB. In both cases charge neutrality is maintained as the number of positive/negative ions equals the number of electrons/holes created.

In Figure 8b the n- and p-type material are brought together to produce an np- (or pn)-junction. There is a very large difference in electrons and holes in each material (in the n-type material the electrons are the majority charge carriers, in a p-type material it is the holes) which causes a diffusion current of charges to flow from one material to the other – the electrons from n- to p-material and holes from p- to n-material. As a result, the electrons and holes recombine at the junction, depleting the region, called the space charge region (SCR), of mobile charge carriers.

The depletion of charges in the SCR leaves only the ionised positive and negative atoms, which are fixed into their lattice positions and cannot move. An internal electric field is created across

the junction by there being excess negative charge on one side and excess positive charge on the other. This electrostatic potential difference (V_{bi}) acts on the charges to move them in the opposite direction to the concentration gradient. An equilibrium is reached when the drift and diffusion currents equal one another.

The drift current can be visualised as balls rolling downhill from high energy to low energy. For hole, because they are positively charged they prefer to go up hill. In solar cells this idea is utilised when combining materials to ensure that the charges flow in the right direction.

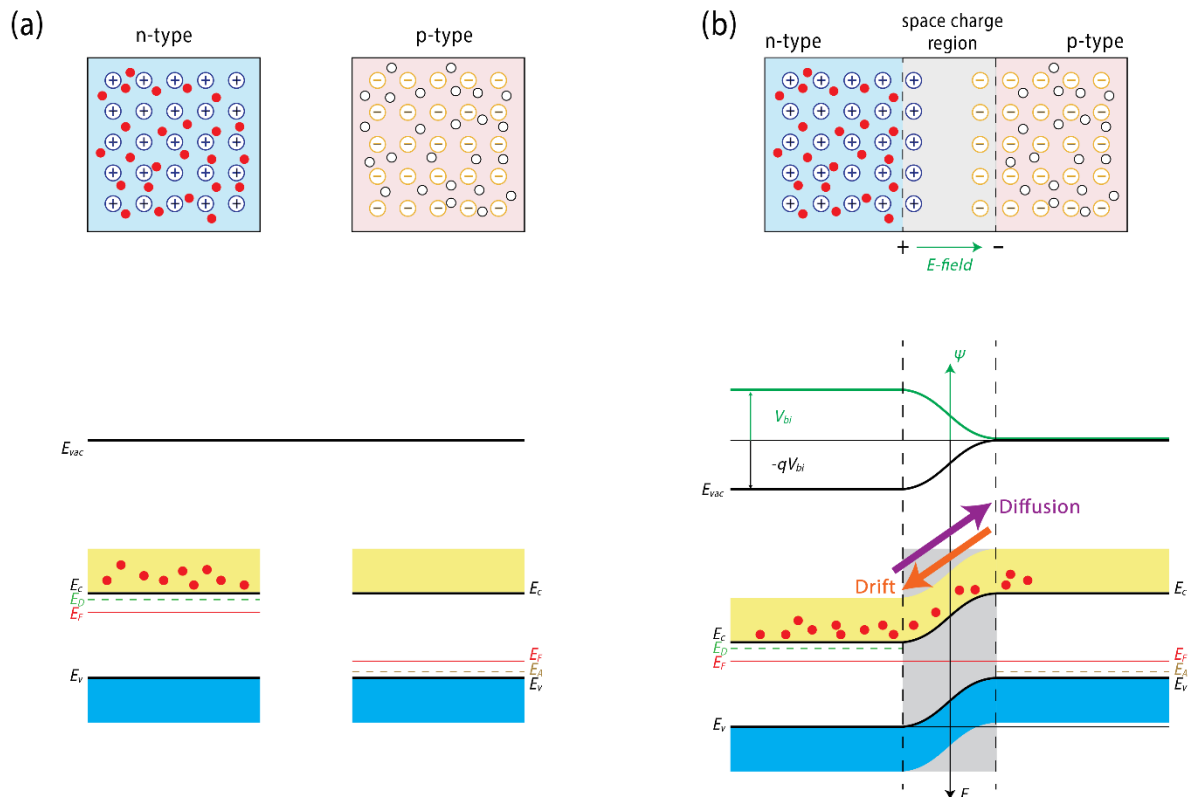


Figure 8. (a) Isolated n- and p-type semiconductors and their band energy level diagrams. (b) A np-junction is produced when the two materials are brought together.

SOLAR CELL: ABSORPTION, GENERATION, SEPARATION, COLLECTION

There are many different solar cell architectures and the variation in design affects the order in which each layer performing a specific function is positioned. However, universal in all solar cells is that irrespective of the architecture they are engineered to perform the four basic processes by which solar cells work, which are: 1) absorption, 2) generation, 3) separation, 4) collection. For the purposes of this report, a general solar cell in the p-i-n structure together with its corresponding band energy diagram is shown in Figure 9. Note, the p-i-n structure indicates the type of doping in each layer (p = p-type, i = intrinsic, n = n-type) and from which direction light enters the solar cells (through the p-type material in this case). The p- and n-type doping of each material on either side of intrinsic layer forms the electric field which can drive the holes and electrons towards then and be transported. Thus hole-transport layers (HTLs) are heavily p-doped so that the holes are the majority charge carrier and can allow other holes to transport through them. Vice versa, electron transport layers (ETLs) are heavily n-doped to allow electron transport.

First, light is *absorbed* by the absorber layer which is enabled by the *generation* of an electron-hole pair after the promotion of an electron from VB to the CB. The electron and hole are attracted electrostatically to each other and so need to be *separated* in order for the charges to later be separately collected. This is achieved by the internal electric field which drives the electrons

towards the ETL and holes towards the HTL, as well as the propensity for the electrons to go down in energy (the CB of the ETL is lower than the CB of the absorber layer) and the holes to go up in energy (as holes are of opposite charge to electrons; the VB of the HTL is higher than the VB of the absorber layer). Once the electrons are in the ETL and the holes are in the HTL, they can then be transported to the cathode and anode, respectively, and *collected*. The ETL and HTL are designed to allow only the relevant charge through whilst blocking the opposite charge, failure to do so seriously diminishes the efficiency of a solar cell. Finally, once the charges have been collected by the electrodes they can be sent to an external circuit and used to do work, e.g. power electrical devices.

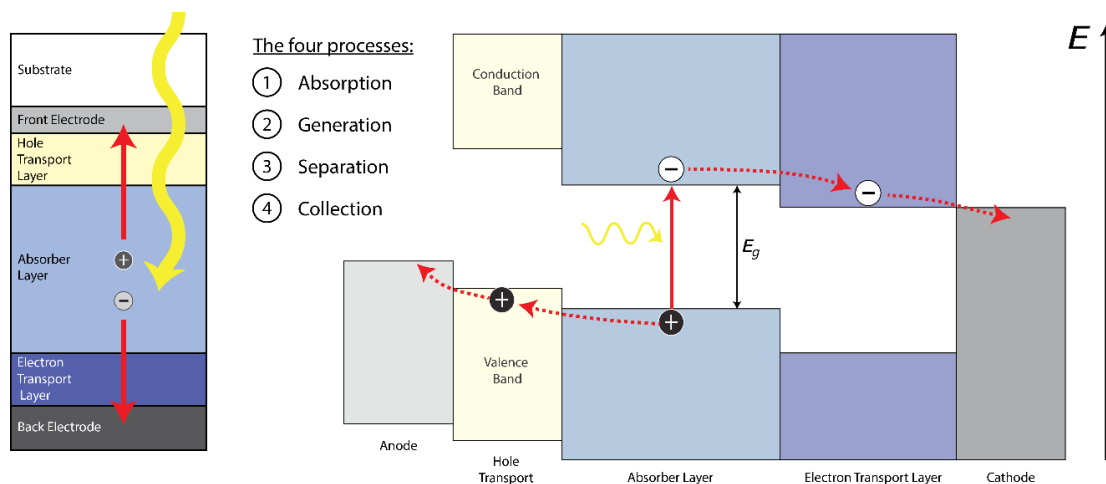


Figure 9. A schematic diagram of a p-i-n solar cell and its band energy level diagram.

PEROVSKITE SOLAR CELL

Perovskites, at least Pb-based perovskites, are intrinsic semiconductors [19] and so the solar cells take the p-i-n (as shown above in Figure 9) or n-i-p configuration. Various materials can be used in a perovskite solar cell and a few common materials are shown in Figure 10. For the purposes of this report only the anode, HTL, and perovskite absorber layer are examined in detail.

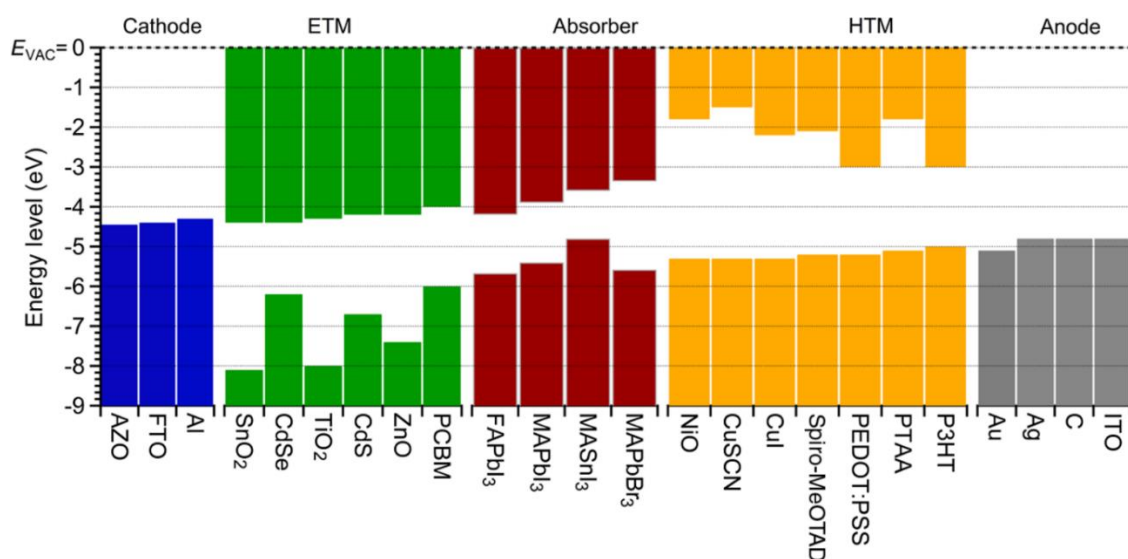


Figure 10. Band energy level diagram of various materials used in perovskite solar cells. [20]

Perovskite Absorber Layer

Perovskites used for PV can be organic-organic, inorganic-inorganic or a hybrid organic-inorganic material, though in general they take the hybrid form. In hybrid perovskites, the A cation is an

organic cation (most often methylammonium, CH_3NH_3^+), the B cation is an inorganic cation (usually Pb) and the X anion(s) is a halide (typically I, often with a small fraction of Cl or Br). A feature of perovskites is the ability to change its band gap *via* composition control. For example, in $\text{CH}_3\text{NH}_3\text{PbX}$ the band gap can be tuned from 3.2 eV when X is entirely Cl, to 1.6 eV if only I is used [21]. Even smaller band gaps can be achieved by changing the organic cation, for instance, if formamidinium ($\text{H}_2\text{NCH}=\text{NH}_2^+$) or ethylammonium ($\text{CH}_3\text{CH}_2\text{NH}_3^+$) is used instead of methylammonium (CH_3NH_3), or if for the inorganic cation Pb is replaced with Sn. [21] The band gap tuneability is useful for achieving good band alignment with other materials in the solar cell or for setting the band-gap to an energy whereby it can absorb a specific part of the spectrum. An added effect of using mixtures of cations, e.g. the triple cation perovskite $\text{Cs}_{0.05}(\text{MA}_{0.17}\text{FA}_{0.83})_{0.95}\text{Pb}(\text{I}_{0.27}\text{Br}_{0.3})$ used in this report, is that it can increase the stability of the solar cell against degradation. [22]

The ability to tune the perovskite band-gap is useful if the perovskite solar cell is to be used in a tandem solar cell, e.g. perovskite top cell and c-Si bottom cell (Figure 11). In such devices, the perovskite would be made with a large band gap so as to absorb the high-energy light whilst letting the lower energy light through to the low band gap bottom cell to be absorbed. This allows tandem solar cells to absorb more of the incident light than single junction solar cells, which cannot utilise the excess energy greater than the band-gap of the material when high energy light is absorbed. [23]

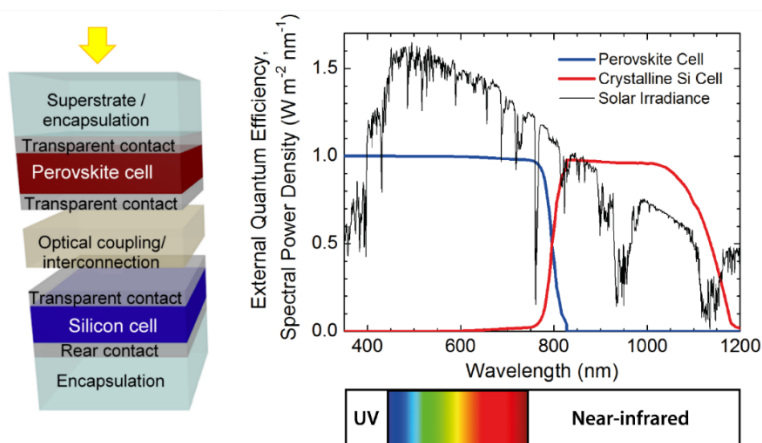


Figure 11. A perovskite/silicon tandem solar cell. Using the two types of solar cells in a tandem configuration can enable a larger part of the incident solar spectrum to be converted to electricity, thus increasing the overall efficiency compared each cell on their own. [23]

Anode

Though PSCs could use Ag or Au as the top electrode, similar to how c-Si solar cells use busbars of Ag to collect charges, this would lead to shading losses and reduced current as the light would be reflected or absorbed by the electrode and would not reach the perovskite layer. To avoid such losses, it is common to use indium tin oxide (ITO) as the top electrode as it is transparent in the visible part of the spectrum whilst also being effective at conducting charges. Top electrodes which use transparent and conductive materials such as ITO are also often referred to by another name of transparent conductive oxides (TCO).

Hole Transport Layer

As mentioned in the introduction, HTLs in perovskite solar cells can be either organic materials such as PEDOT:PSS, PTAA, P3HT and Spiro-MeOTAD, or inorganic materials such as NiO, CuI, and CuSCN. A general trend has been to try to replace organic HTLs with inorganic HTLs for reasons such as reducing cost, improving hole mobilities and improving compatibility with other processing steps. In this report, p-a-SiOx:H is investigated to see whether it can be used as a HTL with the goal of addressing the issues just mentioned.

Whereas c-Si has high manufacturing costs due to the need to make very pure and defect free wafers, hydrogenated amorphous Si (a-Si:H), and by extension p-a-SiO_x:H, has low manufacturing costs for the exact opposite reason of it not needing to be perfectly crystalline. Rather than slowly growing an ingot from molten Si, a-Si can be rapidly deposited *via* vacuum deposition, e.g. PECVD, which enormously decreases the amount of energy used in fabrication. Because Si is a hugely abundant and cheap material, by removing a large part of the energy required to deposit it, what is left is a relatively cheap process. Compared to other more experimental HTLs, p-a-SiO_x:H has the advantage that the manufacturing equipment and know-how is already in place and can be applied at industrial scales. This could be highly beneficial in terms of potential future commercialisation of perovskite solar cells as new manufacturing equipment would not need to be developed specifically for depositing the HTL, reducing capital and R&D costs.

p-a-SiO_x:H possesses a wide band-gap that can be tuned depending on the amount of oxygen doping. [24] Starting at a band gap of 1.8 eV for p-a-Si:H, the band gap could be theoretically go all the way up to 9.0 eV for pure SiO₂ (Figure 12). A band gap of 9.0 eV is far too high for a HTL as it causes the material to behave as an insulator, completely block any current going through, so a much lower band gap of around 2.3 eV would be more feasible. 2.3 eV equates to 539 nm and so light with wavelengths higher than ~539 nm would pass through the HTL, fulfilling the requirement of the HTL being transparent, at least for majority of the solar spectrum.

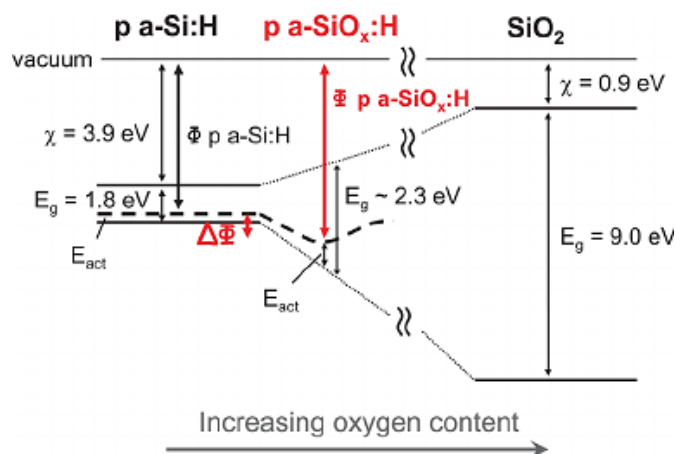


Figure 12. The band energy level diagram of p-a-Si:H and SiO₂. By varying the oxygen concentration the band gap can be tuned from 1.8 eV for p-a-Si:H to 9.0 eV for SiO₂. [24]

Figure 13 shows the band energy level diagram of the triple-cation perovskite, Cs_{0.05}(MA_{0.17}FA_{0.83})_{0.95}Pb(I_{0.27}Br_{0.3}), and p-a-SiO_x:H, individually and when brought together. In bringing the two materials together the Fermi levels align leading to the p-a-SiO_x:H bands being raised. As the VB of the p-a-SiO_x:H is now higher than the VB of perovskite, this will create a drift current promoting hole extraction. Theoretically, p-a-SiO_x:H shows promise as a HTL in perovskite solar cells.

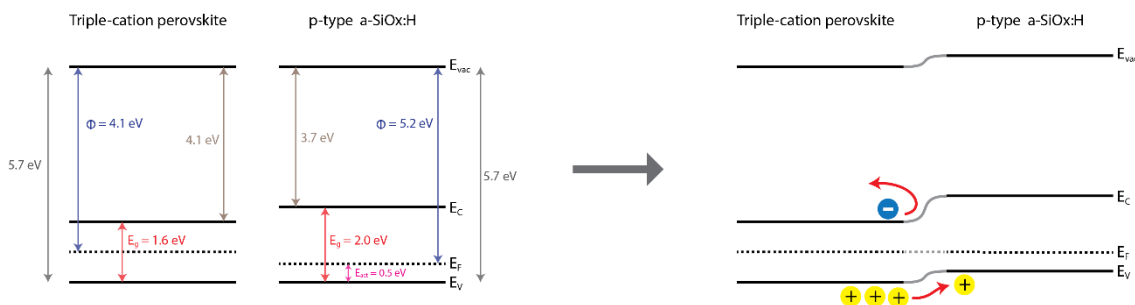


Figure 13. The band energy diagram of triple-cation perovskite and p-a-SiO_x:H isolated (left) and when brought together (right).

3. RESEARCH PROPOSAL

As a first step, the reference Cu:NiOx HTL was replaced by p-a-SiOx:H in order to investigate whether p-a-SiOx:H could be used as a HTL in perovskite solar cells (Figure 14). Further experiments were later conducted which incorporated different cell architectures, however, these are described in more detail in the Results & Discussion section.

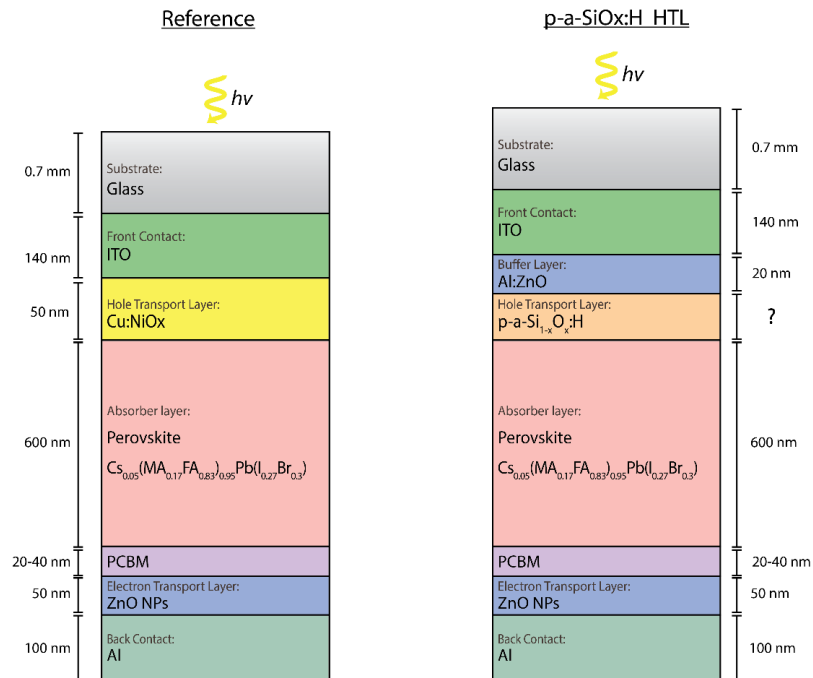


Figure 14. Proposed solar cell design of reference (left) and using p-a-SiOx:H as HTL (right).

4. FABRICATION & CHARACTERISATION TECHNIQUES

To fabricate and characterise the solar cells various techniques were required which are described in the following section.

RF MAGNETRON SPUTTER DEPOSITION

RF Magnetron sputter deposition is a common physical vapour deposition technique used to deposit thin-films of metals, alloys and compounds. Advantageous characteristics of the technique are that the deposition is fast, homogenous and produces high quality thin-films with precise control of its thickness, low temperatures are involved, no dangerous gases are used and there is a relatively low running cost. [25] Because of this, RF Magnetron sputtering has become commonplace in the fabrication of microelectronics, solar cells, and other high-tech industries. [26]

RF Magnetron sputtering utilises a radio-frequency wave to ionise gas atoms, forming a plasma. The electric field placed between the anode and cathode causes the ions to be accelerated towards the target, leading to a build-up of positive charge on the target surface. As the positive charge increases, in order to decrease the positive charge, atoms of the target are ejected which can then deposit on the substrate. The “Magnetron” is a strong magnet used to confine the plasma electrons within a toroidal orbit around the magnetic field lines in the plasma. As the electrons cannot escape the plasma, a high density of electrons is maintained which increases the possibility of collision with atoms to generate new ions and thus sustain the plasma. As a result, less gas (which is often argon and is expensive) and much lower electric field is required for the plasma, reducing cost and potential damage to the deposited material. [25]

In this report, RF Magnetron sputtering was used to deposit ITO and ZnO.

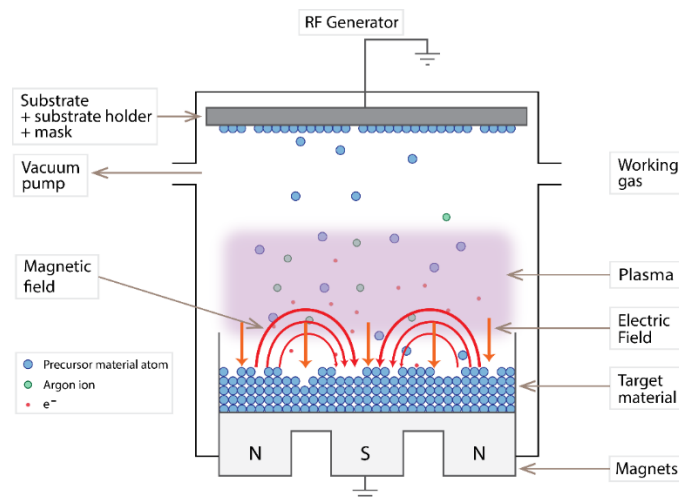


Figure 15. Schematic diagram of RF Magnetron Sputter Deposition. [27]

PLASMA ENHANCED CHEMICAL VAPOUR DEPOSITION (PECVD)

Plasma-Enhanced Chemical Vapour Deposition (PECVD) is a chemical vapour deposition process used to deposit thin-films from a gaseous state (vapour) onto a solid. The mode of operation of PECVD begins by first introducing reactant gases, with argon as the carrier gas, into the chamber via a shower head. The shower head (a perforated metal plate) is designed so as to enable a more uniform distribution of reactant gas flow over the sample surface. Application of an RF potential between the showerhead and the bottom electrode then generates a plasma. The energetic electrons in the plasma can ionize or dissociate reactant gas molecules to generate more

chemically reactive species, which then further react to form the solid deposition material on top of the substrate. As plasma is providing some of the energy to dissociate the reactant molecules, much lower temperatures are required than with purely thermal processing methods which offers advantages such as lower operating costs and less material damage. The deposition rate can be adjusted by changing the temperature or the RF potential, however, this will also affect the material properties of the deposited thin-film. [28]

In this report, PECVD to deposit p-a-SiO_x:H and p-a-Si:H.

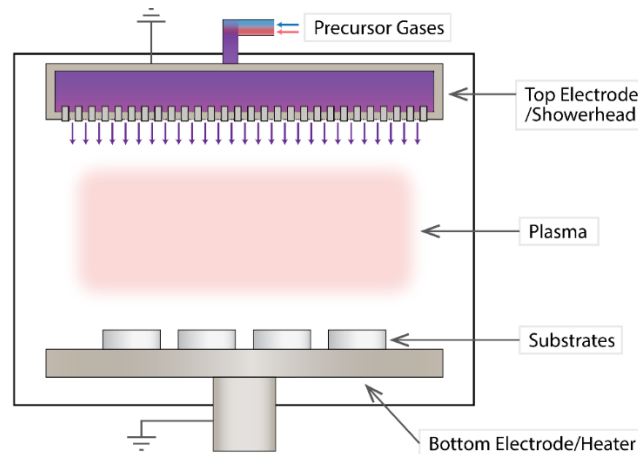


Figure 16. Schematic diagram of Plasma-Enhanced Chemical Vapour Deposition.

SPIN-COATING

Spin-coating is a procedure used to deposit thin uniform films on flat substrates. By applying a solution of the coating material to the middle of the substrate and rotating it at high speed, the centrifugal force causes the liquid to spread out over the surface. The liquid film becomes thinner the longer the duration of rotation and the faster the speed of rotation and so a precise control of the thickness can be achieved by varying these two parameters. For the deposition of perovskite, an anti-solvent is applied to the coated liquid whilst the substrate is rotating in order to cause the perovskite to precipitate as a solid from solution onto the substrate. Subsequently, the substrate can then be removed and further processing steps carried out, e.g. drying, annealing. [29]

In this report, spin-coating was used to deposit perovskite, PCBM and ZnO NPs.

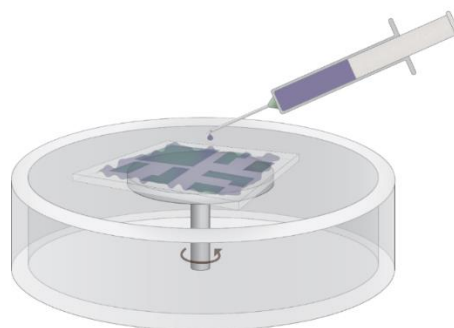


Figure 17. Schematic diagram of Spin-Coating.

THERMAL EVAPORATION

Thermal evaporation is a very simple form of Physical Vapour Deposition used to deposit thin-films. A material is heated by a hot filament coil such that the surface atoms of the material obtain

sufficient energy to leave the surface. The vaporous atoms can then traverse the vacuum chamber until they collide with the substrate, thus condensing and being deposited.

In this report, thermal evaporation was used to deposit the Al back electrode.

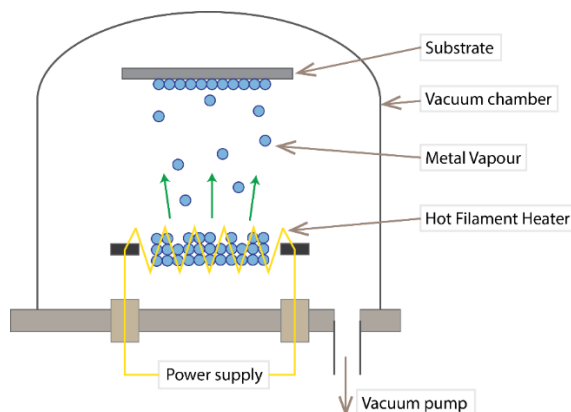


Figure 18. Schematic diagram of Thermal Evaporation.

KELVIN PROBE

The Kelvin Probe (KP) is a non-contact, non-destructive vibrating capacitor device used to measure the work function difference between a conducting specimen and a vibrating tip. The WF is defined as “the energy required to remove an electron originally at the Fermi level (E_F) and place it at rest at a point in free space just outside the surface, *i.e.* at E_{VAC} .” The WF consists of a bulk and surface contribution. The bulk contribution derives from the electronic density and density of states in the solid and the surface contribution corresponds to an additional potential step originating from the redistribution of charges at the surface of the solid. [30] The two terms cannot be separated experimentally and the KP simply gives the total WF.

Note, it is necessary to place electrical tape in contact with the sample so that any charge that is induced by the vibrating probe is discharged. This is because charge on the surface of the sample will affect the contact potential difference (CPD) measured and thus the subsequently determined WF.

In this report the WF of various materials was measured:

p-a-SiOx:H, p-a-Si:H, c-Si, ITO, IO:H, CuGaOx, CuSCN, CuO, CuI, NiOx.

The Kelvin probe measurements on p-a-SiOx:H is discussed in the section “Results & Discussion – Characterisation of p-a-SiOx:H”. The WF values of the other materials are given in Appendix A.

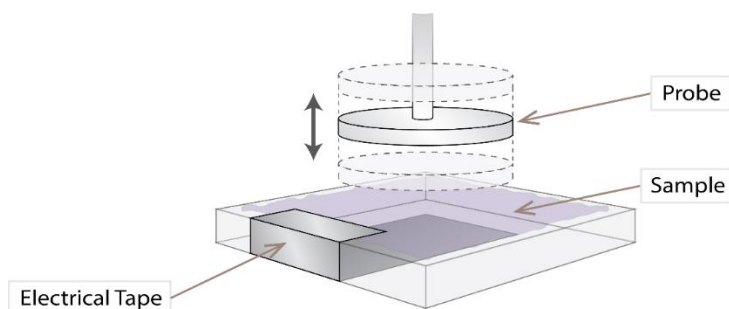


Figure 19. Schematic diagram of the Kelvin Probe.

DARK CONDUCTIVITY & ACTIVATION ENERGY

The temperature dependence of the current flowing through a material can be used to determine the activation energy of the material. In order to be able to do this, metal contacts are first deposited onto the material, then a voltage is applied across using two electrodes and substrate temperature varied by a heater underneath it.

In this report, the temperature dependent conductivity of p-a-SiO_x:H was measured.

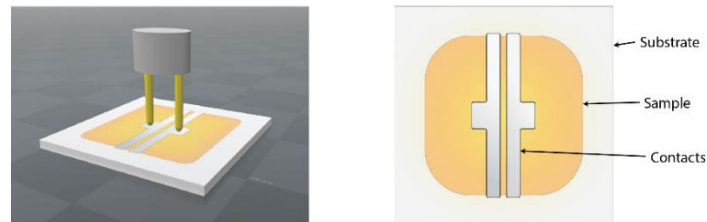


Figure 20. Schematic diagram of the substrates and deposited contacts used to measure the dark conductivity and activation energy.

HALL PROBE

When electric current flows through a conducting material in a magnetic field, a transverse force is exerted on the charge carriers by the magnetic field altering their direction of travel. As electrons and holes possess opposite charges they are deflected in opposite directions, leading to a build-up of charges on opposite sides of the material, thus creating a voltage. This is known as the Hall effect (Figure 21a).^[31] A Hall probe can measure the voltage generated and from this calculate various parameters such as the concentration and mobility of free carriers. In addition, due to the Hall probe being set up in the Van der Pauw configuration (Figure 21b), the resistivity and sheet resistance of the material could also be determined.

In this report, the Hall probe was used to measure the properties of ITO. It was not possible to measure the properties of other materials used in this report such as p-a-SiO_x:H, ZnO, *etc.* as they were not conducting enough.

The properties of ITO measured using the Hall Probe are given in Appendix B.

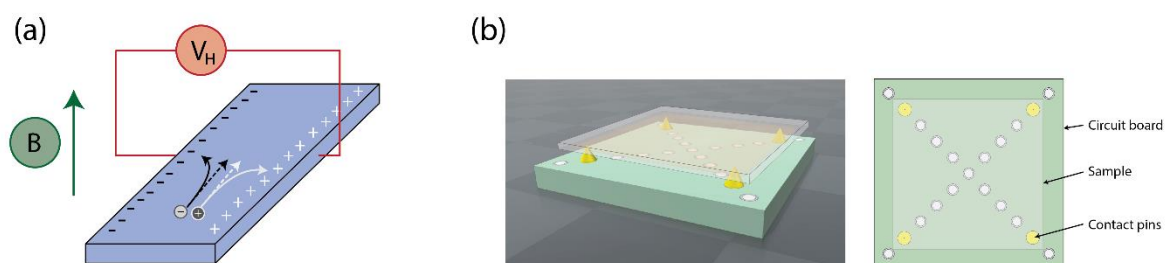


Figure 21. (a) Hall effect. (b) Schematic diagram of the Hall Probe measurement set-up.

4-POINT PROBE

The 4-point probe is an electrical impedance measuring technique that uses separate pairs of current-supplying (source) and voltage-sensing (sense) electrodes. The current supplied via the source electrodes causes the voltage to drop across the sense electrodes according to Ohm's law $V=IR$, thus the resistance can be measured.

In this report the 4-point probe was used to measure the sheet resistance of ITO, as a supplement to verify and compare the sheet resistance measured using the Hall probe.

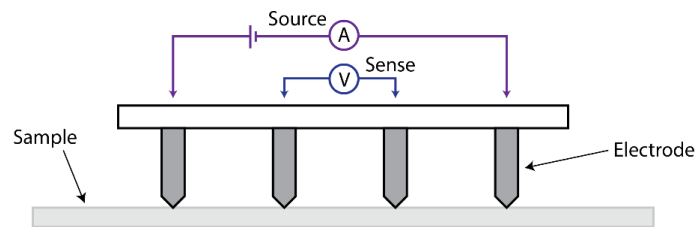


Figure 22. Schematic diagram of the 4-Point Probe.

IV

One of the most basic ways to characterise a solar cell's performance is by measuring its current (I) vs. voltage (V) characteristics. As a solar cell is fundamentally a diode, a non-linear IV curve is observed. Important parameters which characterise the solar cell are the short circuit current (I_{sc}), open circuit voltage (V_{oc}), fill factor (FF), maximum power point (MPP), and efficiency (%).

Short Circuit Current, I_{sc} :

The I_{sc} is the current which flows through the solar cell when the voltage across the solar cell is zero, *i.e.* when it is short circuited, and comes about due to the generation and collection of light-generated charge carriers.

Open Circuit Voltage, V_{oc} :

The V_{oc} is the maximum voltage available from the solar cell, occurring at zero current, and which corresponds to the amount of forward bias on the solar cell as a result of the bias across the solar cell junction with the light-generated current.

Maximum Power Point, MPP:

The power generated by a solar cell is the product of its voltage and current ($P=IV$). The I_{sc} is the maximum current and the V_{oc} is the maximum voltage of the solar cell, however, at each of these points the other value is zero and so the power is zero. Along the IV curve the current and voltage are non-zero and at a particular point the product of the two will produce a maximum power value known as the maximum power point, MPP. Thus, the ideal operation of the solar cell is defined to be at the MPP.

The MPP is also equivalent to the efficiency of the solar cell. Because the units for the MPP are mW/cm^2

Fill Factor, FF:

The FF is a parameter which effectively measures the "squareness" of an IV curve. It is related to the MPP as the FF is the ratio of the MPP (**Figure**, red shaded area) to the product of V_{oc} and I_{sc} (**Figure**, blue shaded area). An efficient solar cell will have a high FF because the MPP will be close to the product of V_{oc} and I_{sc} .

Efficiency, η :

The efficiency of a solar cell is defined as the ratio of energy output from the solar cell to input energy from the sun. The power output from the solar cell ($FF \times I_{sc} \times V_{oc}$) is in fact the MPP, whereas when measuring solar cells "standard test condition" of AM1.5 ($1000 W/m^2$) at 25 °C is used for the input power.

$1000 W/m^2$ is equivalent to $100 mW/cm^2$. As the MPP (units in mA/cm^2) is the measure of output power and efficiency is the ratio of the MPP over $100 mW/cm^2$, it is the case that the efficiency as

a percentage is thus equivalent to the MPP. From looking at the MPP one can thus easily know what the efficiency of the solar cell is.

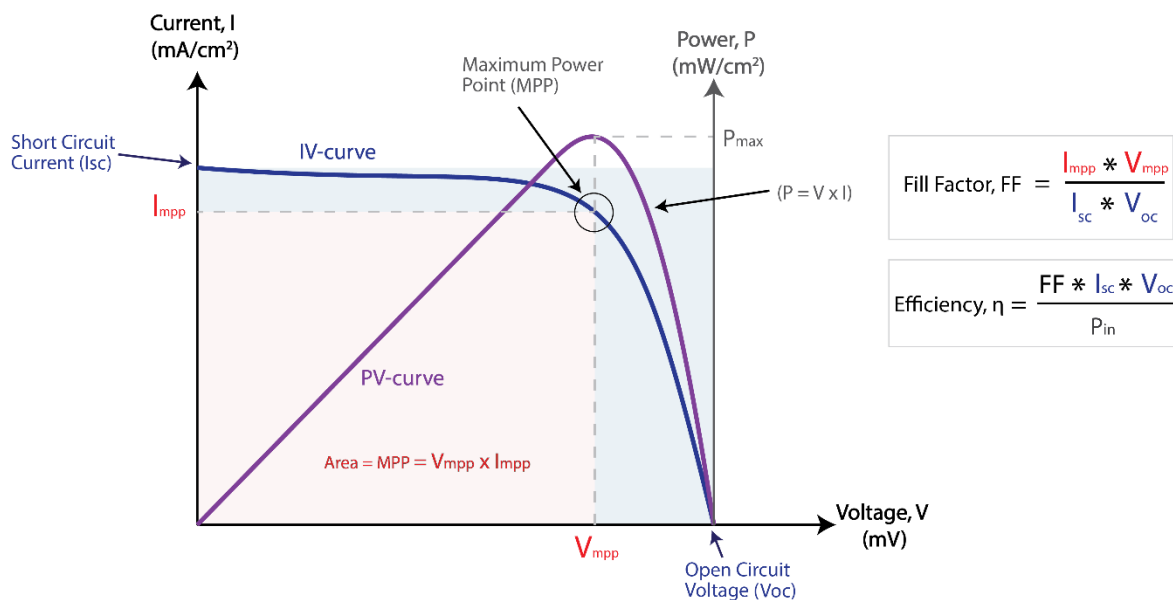


Figure 23. A typical IV-curve of a solar cell.

CONTACT ANGLE MEASUREMENTS

A liquid which forms favourable interactions with the solid will spread out across the surface, giving a small (or zero) solid/liquid contact angle (Figure 24a). Vice versa, a liquid which does not form favourable interactions with the solid will not spread out across the surface and will remain as a droplet on the surface, giving a large contact angle (Figure 24b). A polar liquid and polar solid, or, an apolar liquid and apolar solid, will form favourable interactions whereas apolar-polar interactions are unfavourable. Different liquids have different polar/dispersive (apolar) components to their surface tension (*i.e.* can form polar or apolar interactions to different degrees) and so will give different contact angles when placed on a solid. By using a variety of liquids, a range of contact angles can be measured which are then used to calculate the surface energy of the solid. If the polar and dispersive components of the liquid surface tension are known, using Owen-Wendt Theory the surface energy of the solid can also be broken down into its polar and dispersive components.^[32]

In this report contact angle measurements were performed on p-a-SiO_x:H, ITO and ZnO.



Figure 24. (a) A liquid which wets the surface well creates a small solid-liquid contact angle. (b) A liquid which does not like to wet the surface creates a large solid-liquid contact angle.

5. EXPERIMENTAL SECTION

FABRICATION OF SOLAR CELLS

Figure shows the processing steps required to fabricate the solar cells in this report. For the most part, each cell was fabricated in the same way except for when the HTL was to be deposited in Step 2. A detailed explanation of each step is described in the following section.

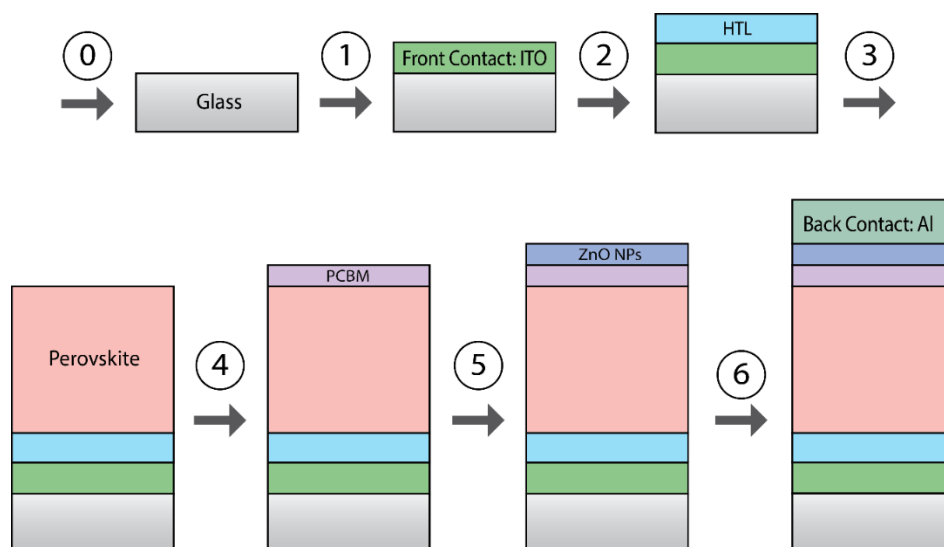


Figure 25. Overview of the steps required to fabricate the perovskite solar cells. Note, the cells are fabricated upside down, i.e. from the glass which receives the incoming light. This is known as the inverted structure.

Step 0 – Cleaning of the glass substrates

Corning Eagle XG Slim Glass Substrates (30 x 30 x 0.7 mm) were used as the substrates. Prior to any subsequent processing steps the substrates were washed by ultra-sonication in a series of liquids:

- 1) The substrates were placed in a solution of Extran MA02 (25 mL) diluted in demi water (175 ml) and ultra-sonicated (5 mins).
- 2) The substrates were removed, rinsed with demi water and then ultra-sonicated in clean demi water (5 mins).
- 3) The substrates were removed, washed with isopropanol and then ultra-sonicated in clean isopropanol (5 mins).

Finally, the substrates were removed and dried (compressed N₂)

Step 1 – Deposition of ITO

ITO was used as the front electrode in the solar cells and had a thickness of 140 nm.

The ITO was deposited onto the glass substrates using RF Magnetron Sputtering. The sputtering parameters were:

Thickness (nm)	Target Material	Target Distance (cm)	Power (W)	Substrate Temp. (°C)	Pressure (mbar)	Ar (with 2.5 % O ₂) flow (cm ³ /min)	Deposition Rate (nm/s)	Deposition Time (s)
120	In ₂ O ₃ /SnO ₂ (90/10 wt%)	18	54	RT	0.003	20	0.14	857

Step 2 – Deposition of Hole Transport Layer

Reference Cell: Glass / ITO / NiOx NPs / Perovskite / PCBM / ZnO NP / Al

In the reference cell, a NiOx NPs with a thickness of ~50 nm was used as the HTL.

Prior to the NiOx NP deposition, the glass substrates were subjected to a UV + ozone treatment for 30 mins. The NiOx NPs were then deposited *via* spin-coating at 4000 rpm for 60 s.

Reference Cell: Glass / ITO / Cu:NiOx / Perovskite / PCBM / ZnO NP / Al

In the reference cell, a compact layer of Cu:NiOx with a thickness of ~50 nm was used as the HTL.

Prior to the Cu:NiOx deposition, the glass substrates were subjected to a UV + ozone treatment for 30 mins. The Cu:NiOx was then deposited *via* spin-coating using the following parameters:

The Cu:NiOx solution was quickly injected onto the substrate and spun at 4000 rpm for 60 s. The substrate was then removed and annealed at 120 °C for 1 min inside the glovebox, then removed from the glovebox and annealed at 290 °C for 15 mins inside a fume cupboard.

Cell Design 1: Glass / ITO / Al:ZnO / p-a-SiOx:H / Perovskite / PCBM / ZnO NP / Al

Al:ZnO was used as a buffer layer and p-a-SiOx:H as the HTL. The Al:ZnO was 20 nm and the p-a-SiOx:H was 10 and 20 nm.

The Al:ZnO was deposited onto the glass substrates *via* RF Magnetron Sputtering using the following parameters:

Thickness (nm)	Target Material	Target Distance (cm)	Power (W)	Substrate Temp. (°C)	Pressure (mbar)	Ar (with 25 % O ₂) flow (cm ³ /min)	Deposition Rate (nm/s)	Deposition Time (s)
20	Al ₂ O ₃ /ZnO (2/98 wt%)	18	108	RT	0.003	6	0.016	1250

The p-a-SiOx:H was then deposited onto the Al:ZnO *via* PECVD using the following parameters:

Thickness (nm)	Power (W)	Electrode Distance (cm)	Substrate Temp. (°C)	Pressure (mbar)	H ₂ flow (cm ³ /min)	SiH ₄ flow (cm ³ /min)	B ₂ H ₆ flow (cm ³ /min)	CO ₂ flow (cm ³ /min)	Deposition Rate (nm/s)	Deposition Time (s)
10	80	12	190	8	200	1	0.025	1.1	0.10	100
20	80	12	190	8	200	1	0.025	1.1	0.10	200

Cell Design 2: Glass / ITO / Al:ZnO / p-a-Si:H / Perovskite / PCBM / ZnO NP / Al

Al:ZnO was used as a buffer layer and p-a-Si:H as the HTL. The Al:ZnO was 20 nm and the p-a-Si:H was 3, 6 and 10 nm.

The Al:ZnO was deposited onto the glass substrates *via* RF Magnetron Sputtering, as described previously.

The p-a-Si:H was then deposited onto the Al:ZnO *via* PECVD using the following parameters:

Thickness (nm)	Power (W)	Electrode Distance (cm)	Substrate Temp. (°C)	Pressure (mbar)	H ₂ flow (cm ³ /min)	SiH ₄ flow (cm ³ /min)	B ₂ H ₆ flow (cm ³ /min)	Deposition Rate (nm/s)	Deposition Time (s)
3	3	14	180	0.79	200	20	8	0.17	17
6	3	14	180	0.79	200	20	8	0.17	34
10	3	14	180	0.79	200	20	8	0.17	59

Cell Design :Glass / ITO / Al:ZnO / p-a-SiOx:H / Cu:NiOx / Perovskite / PCBM / ZnO NP / Al

Al:ZnO was used as a buffer layer and p-a-SiOx:H and Cu:NiOx were used as the HTL. The Al:ZnO was 20 nm, the p-a-SiOx:H was 20 nm, and the Cu:NiOx was ~50 nm.

The Al:ZnO was deposited onto the glass substrates *via* RF Magnetron Sputtering, the p-a-SiOx:H deposited onto the Al:ZnO *via* PECVD, and then the Cu:NiOx was deposited onto the p-a-SiOx:H *via* spin-coating, as described previously.

Step 3 – Deposition of Triple Cation Perovskite - $\text{Cs}_{0.05}(\text{MA}_{0.17}\text{FA}_{0.83})_{0.95}\text{Pb}(\text{I}_{0.27}\text{Br}_{0.3})$

The triple cation perovskite $\text{Cs}_{0.05}(\text{MA}_{0.17}\text{FA}_{0.83})_{0.95}\text{Pb}(\text{I}_{0.27}\text{Br}_{0.3})$ was used as the absorber layer. In each cell the thickness of the perovskite layer was 600 nm.

Preparation of perovskite solution

To form the perovskite solution first two precursor solutions were created.

Solution 1: PbI_2 (2.88 g), FAI (0.86 g), PbBr_2 (0.184 g) and MABr (0.112 g) were added to DMF (4.5 mL) and DMSO (0.5 mL), and stirred (1 h, RT).

Solution 2: CsI (0.195 g) was added to DMSO (0.5 mL) and stirred (1 h, RT).

After stirring for 1 h, Solution 1 (0.2 mL) was added to Solution 2 (0.2 mL) and left stirring overnight at RT.

Spin-coating perovskite solution

N.B. For the reference cells using Cu:NiOx as the HTL, prior to the deposition of the perovskite the glass substrates were subjected to a UV + ozone treatment (30 mins). For all except one set of cells using p-a-SiOx:H as the HTL, there was no UV + ozone treatment before perovskite deposition.

In a N_2 glovebox, the perovskite solution was quickly injected onto the substrate (onto the HTL) and spun at: i) 2000 rpm for 20 s, then, ii) 5000 rpm for 10 s, then, iii) 2000 rpm for 30 s. During the second step, chlorobenzene (170 μL) as the anti-solvent to make the perovskite precipitate out of solution. The substrates were then annealed (100 °C, 10 mins).

Step 4 – Deposition of PCBM

PCBM was used as an interfacial layer between the perovskite and ZnO NPs in order to planarise the perovskite surface and more effectively extract the electrons. The thickness of the PCBM layer varied depending on the morphology of the perovskite, but was on average around 20 - 40 nm.

Preparation of PCBM solution

PCBM (40 mg) was added to chlorobenzene (2 mL) and left stirring overnight (60°C)

Spin-coating PCBM solution

In a N_2 glovebox, the PCBM solution was quickly injected onto the substrate (onto perovskite layer) and spun at 1300 rpm for 55 s, then 3000 rpm for 30 s.

Step 5 – Deposition of ZnO NPs

ZnO NPs were used as the ETL. The thickness of the ZnO NP layer was around 50 nm.

Spin-coating ZnO NPs

ZnO NPs (25 nm, 10 mg/mL in butan-1-ol) was quickly injected onto the substrate (onto PCMB) and spun at 3000 rpm for 50 s.

Step 6 – Deposition of Al

Aluminium was used as the back electrode in the solar cells and had a thickness of 100 nm.

The Al was deposited using thermal evaporation using the following parameters:

A mask was placed into the substrate holder followed by the substrates, and the holder was placed into the evaporator with the substrates facing down. Several pellets of Al were added to the boat and heated so as to evaporate. The pressure of the chamber was 1×10^{-6} mbar and the deposition rate was 0.1 nm/s

6. RESULTS & DISCUSSION

CHARACTERISATION OF P-A-SiOx:H

Before fabricating solar cells using p-a-SiOx:H as the HTL, it was important to first characterise the properties of the material itself. The band energy level diagram in Figure 13 predicted that upon bringing p-a-SiOx:H and perovskite together, the bands would align favourably in a way that would promote drift of the holes into the VB of the HTL whilst at the same time blocking electrons from entering the CB of the HTL. However, this relied on the fact that the p-a-SiOx:H should have a wide band-gap, E_g , and high workfunction, ϕ . Should the band-gap and workfunction not be as large as predicted then a good band alignment may not be achieved which could impact the ability of the HTL to perform its function effectively. To characterise p-a-SiOx:H, reflectance and transmittance spectra were obtained, the work function was determined using a Kelvin probe, and activation and dark conductivity measurements were conducted.

REFLECTANCE/TRANSMITTANCE

Figure 26 shows the reflectance and transmittance spectra of a 100 nm thick layer of p-a-SiOx:H deposited on a glass substrate, over the range of 300-1200 nm. For comparison, a 100 nm p-a-Si:H layer is shown also. With respect to reflectance, it is favourable for the HTL to have a very low reflectance so that a maximum amount of light enters the material and the thus solar cell. Once light is in the material the next step is for it to be transmitted without being absorbed. Absorption of light by the HTL will reduce the amount of light that enters the perovskite and so a high transmittance is desirable, particularly in the range of visible light, though absorption of higher energy UV light can be favourable as the HTL would act as a filter for the UV light, preventing it reaching the perovskite where it could otherwise contribute to UV induced degradation mechanisms. As can be seen from the spectra, p-a-SiOx:H outperforms p-a-Si:H in both respects, being less reflective and more transmitting than p-a-Si:H. The reason for this could be due to p-a-SiOx:H having a larger band gap than p-a-Si:H. The larger band gap means higher energy light is required to excite electrons from the VB to the CB. Light which has energy lower than this higher energy now does not have sufficient energy to photo-excite electrons and so passes through the material unabsorbed, giving a higher transmittance.

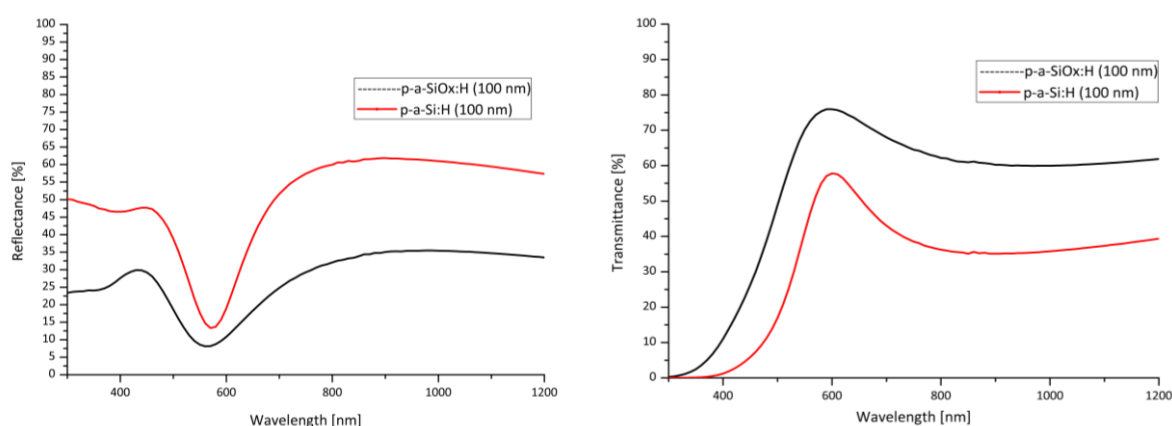


Figure 26. Reflectance (left) and transmittance (right) spectra of p-a-SiOx:H (100 nm). p-a-Si:H (100 nm) is also shown for comparison.

To determine the exact value of the band-gap of each material, Tauc plots can be drawn (Figure 27). Tauc plots involve plotting the absorption coefficient multiplied by the photon energy, raised to the power $1/n$, versus the incident photon energy:

$$(\alpha hv)^{1/n} \text{ vs. } hv$$

where: α = absorption coefficient, h = Planck's constant, ν = frequency, n = is a factor which depends on the type of electronic transition, for an allowed transition in an indirect band-gap material such as p-a-SiOx:H and p-a-Si:H the n factor is 2.

The absorption coefficient can be determined from the transmittance spectra using the Beer-Lambert law, arriving at the equation:

$$\alpha = \ln\left(\frac{1}{T}\right) * \frac{1}{t}$$

where: α = absorption coefficient, T = transmittance, t = thickness.

Using the transmittance spectra and Beer-Lambert law to determine the absorption coefficient however does not produce the most accurate value for the absorption coefficient. This is because it does not take into consideration the reflection of any incident light – it is assumed all incident light enters the material, which is clearly not the case as can be seen from Figure 26. A better way to determine the absorption coefficient would be to use ellipsometry, however, the ellipsometer was broken and thus unavailable for the entirety of the internship.

Finally, once $(\alpha h\nu)^{1/n}$ vs. $h\nu$ has been plotted the linear part of the tail (between ~2.5 - 4.0 eV, Figure 27) can be linearly fitted and the line extended to $y = 0$, whereby the value for the energy at the intersection with the x-axis corresponds to the band-gap of the material. In this way, for p-a-SiOx:H the $E_g = 1.89$ eV and for p-a-Si:H the $E_g = 1.72$ eV. The band-gap for p-a-SiOx:H was lower than the 2 eV that was anticipated, however, it was still higher than for p-a-Si:H indicating that there was at least some oxygen present in the material.

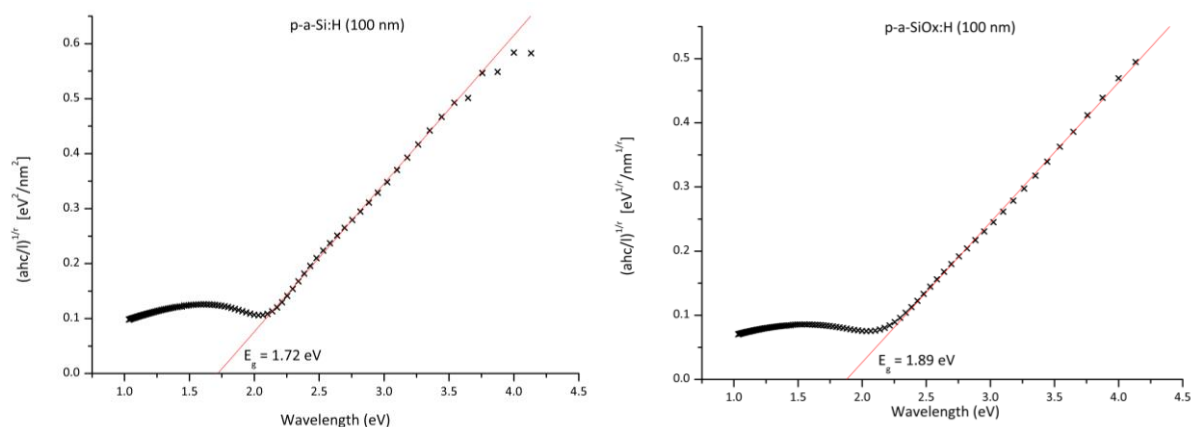


Figure 28. Tauc plots for p-a-Si:H (left) and p-a-SiOx:H (right).

KELVIN PROBE

To measure the work function of a material using a Kelvin probe it is necessary to first create a calibration curve using two reference materials of known work function. This is done by measuring the contact potential difference (CPD) of each material and then plotting the work function vs. the CPD, creating a line. The CPD of the sample is then measured and the WF determined from the calibration curve. For the Kelvin probe measurements in this report the reference materials were aluminium, $\phi = 4.08$ eV [33], and gold, $\phi = 5.1$ eV [33]. The work function of p-a-SiOx:H was determined to be 4.80 eV. For comparison, the work function of p-a-Si:H was also measured and determined to be 4.51 eV.

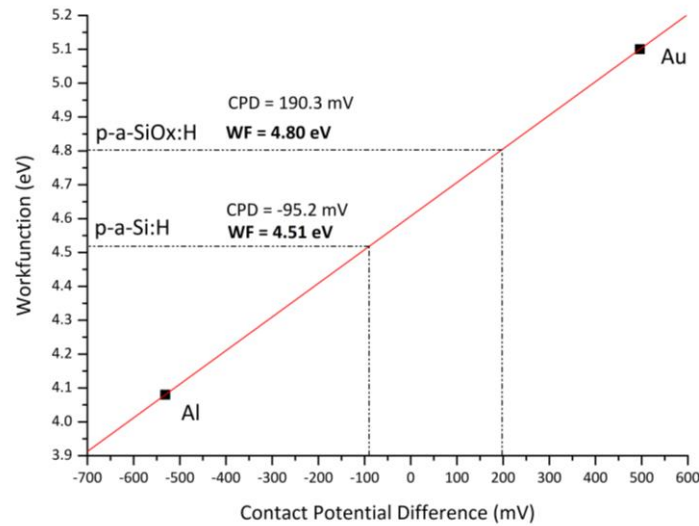


Figure 29. Kelvin probe work function measurements of p-a-SiOx:H and p-a-Si:H.

As was the case with the band gap of each material, the work functions were lower than expected (p-a-SiOx:H; measured = 4.80 eV, expected = 5.2 eV). It could be the case that the measured work function is the actual work function of the material, however, there are a number of other factors encountered when conducting the Kelvin probe measurements which cast doubt on the validity of the result. These factors could be:

- 1) Adsorbed molecules on surface
- 2) Electrical tape did not discharge induced surface charges

Factor 1: Adsorbed molecules on the surface of the material

The WF of a material consists of a bulk and surface contribution. The surface contribution arises because of a “spill-out” of electrons due to a tunnelling effect, creating a built-up of negative charge on the surface which creates a potential step for electrons to travel through to reach E_{vac} , effectively raising the E_{vac} level and thus WF. The distribution of charges on the surface is very sensitive to the atomic arrangement of the surface atoms, *i.e.* the crystallographic orientation, and adsorbed molecules. Adsorbed molecules on the surface compress the surface dipole due to electrostatic repulsion and the Pauli exclusion principle in what is known as the “pillow effect”, thus reducing the WF. [30] This is true for all materials, whether it be the Al or Au references, or the p-a-SiOx:H and p-a-Si:H. It is important that in order to measure the true WF of your material, the surface should be clean and free of adsorbates.

When first conducting the Kelvin probe measurements the KP chamber was flushed for 15 minutes with N_2 . This was thought to be sufficient to remove any adsorbates from the surface, however, as can be seen from Figure 30 (top), this was not sufficient as the WF of the gold reference increases over time after the KP was turned on. It was not immediately clear at the time why the WF was increasing with time, however, after the idea arose that it could be adsorbates desorbing from the surface which was causing the WF to increase, a test was done in which the KP chamber was left flushing over the weekend and then the WF measured again, Figure 30 (bottom). As can be seen, after flushing the KP over the weekend the WF of gold did not increase over time, confirming that indeed it was adsorbed molecules which were responsible for the lower WF values.

Knowing this, all subsequent KP measurements were conducted after the sample material had been flushed for an extended period of time (overnight to days). The WF measurements on various materials then did not change over time, suggesting that a very long N_2 flushing was sufficient to remove adsorbates. However, no other means of verification was possible to confirm

that there were no adsorbates on the surface, it could be the case for p-a-SiOx:H and p-a-Si:H that the adsorbates had a particular affinity for their surfaces and simple flushing with N₂, irrespective of the duration, would not remove the adsorbates. Ideally, a UV + ozone treatment would be performed on the materials to remove adsorbates, either in-situ in the KP chamber or the UV + ozone and KP placed inside a N₂ glovebox, but this was not possible. The UV + ozone equipment was on the other side of the lab from the KP and performing the procedure on the materials would be pointless as transfer of the materials would have been through the open lab atmosphere, thus upon exposure to the air there would be immediate condensation of adsorbates onto the material surface.

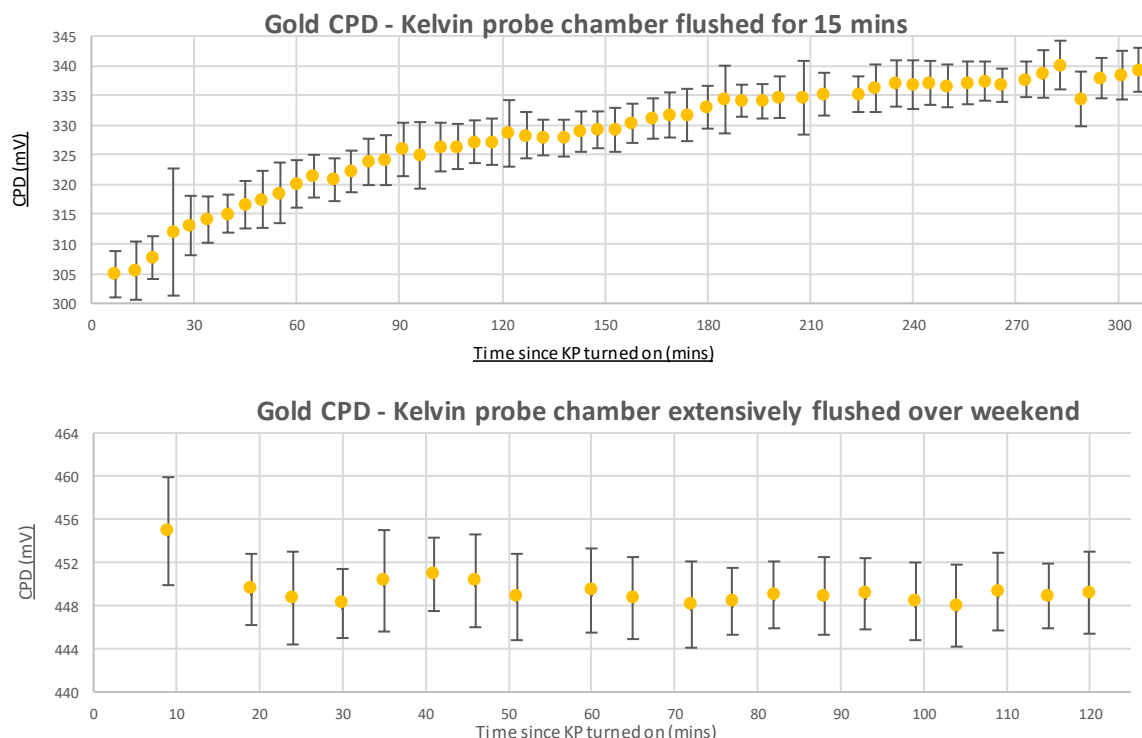


Figure 30. Work function measurements of gold after 15 minutes of N₂ flushing (top) and after a weekend of flushing (bottom).

Factor 2: Electrical tape was insufficient to discharge induced surface charge

The second factor which may influence the measured WF of p-a-SiOx:H and p-a-Si:H could be that the induced surface charges were not sufficiently discharged with the electrical tape. For the KP measurements of ITO and other conductive materials, one strip of electrical tap was sufficient to discharge the charges. This was evident because a good signal could be obtained immediately when setting up the measurement. Furthermore, the WF did not change even when more strips of electrical tape were added around the sample and/or a grounding cable put in contact with the surface. For p-a-SiOx:H and p-a-Si:H however, it was not possible to get a good enough signal when setting up the measurement with only one strip of electrical tape. By placing electrical tape all around the perimeter of the sample so that only a small square the size of the probe was left exposed, a good signal was achieved, suggesting that this sufficient to discharge the surface charges. However, the p-a-SiOx:H and p-a-Si:H have very low conductivity, as was evident from the inability of performing Hall measurements on them as well as the incredibly low current observed in the activation and dark conductivity measurements (next section). The very low conductivity could have the effect that, despite the circumvention of electrical tape, surface charges on the exposed surface underneath the probe could remain there and not be conducted to the electrical tape to be discharged, thus affecting the measured WF value.

Summary

Of the two factors, it seems that the second is more likely to have affected the WF value for p-a-SiOx:H and p-a-Si:H, however, without further tests it is not possible to come to a firm conclusion. Indeed, it may also be the case that the measured WF value is in fact the true value and the lower than expected value is a result of other factors so far not considered. As the WF consists of a bulk and surface contribution, an uneven distribution of boron or oxygen dopants in the materials (boron and oxygen for p-a-SiOx:H, boron for p-a-Si:H) could affect the bulk contribution to the WF if near the surface there is depletion or a high concentration of one or more of the dopants. Alternatively, the surface contribution is highly sensitive to crystallographic orientation and though the two materials are amorphous, the roughness of the surface could have an impact. Both, the composition and surface roughness, are dependent on the deposition conditions which can have batch-to-batch variability.

ACTIVATION ENERGY & DARK CONDUCTIVITY

The p-a-SiOx:H layer should have a high dark conductivity in order to be conductive and conduct the holes. In order to achieve this the activation energy, *i.e.* the energy difference between the VB and the boron acceptor dopant energy level, should be small [34]. A small activation energy would allow electrons to be more easily promoted from the VB to the acceptor levels, leaving holes behind in the VB to conduct charge.

The following equation gives the temperature dependant carrier concentration and can be used to determine the activation energy:

$$n(T) = C * \exp\left(-\frac{E_A}{kT}\right)$$

where: $n(T)$ = temperature dependant carrier concentration, C = prefactor, E_A = activation energy, k = Boltzmann's constant, and T = temperature.

As the carrier concentration is proportional to current, the carrier concentration can be replaced by the current, I . Then, taking the logarithm of this equation allows us to form an Arrhenius plot of $\ln(I)$ vs. $1/T$, and the activation energy can be deduced from the gradient:

$$\ln(I) = \ln C - \frac{E_A}{k} * \frac{1}{T}$$

where: $\ln(I)$ = logarithm of the current = logarithm of carrier concentration, $\ln C$ = logarithm of the prefactor, E_A = activation energy, k = Boltzmann's constant, and T = temperature.

In order to measure the activation energy, metal contacts need to be deposited on the material of interest, as shown in the Figure 31. For the 1st attempt at measuring the activation energy of p-a-SiOx:H, the contacts were deposited by RF Magnetron Sputtering. Figure 31 (left) shows the temperature dependence of the current of this first measurement. As can be seen from the graph, the current (black line) decreases with increasing temperature (purple line), meaning the resistance increases with increasing temperature. This behaviour is characteristic of a metal rather than a semiconductor such as p-a-SiOx:H. The explanation as to why this could have happened comes down to the processing conditions during the sputtering. RF Magnetron sputtering employs a plasma for its operation which can encroach under the mask of the contact, leading to blurring of the edges of the deposited material. As the contacts were close together, it seems that a very thin layer of aluminium was deposited on the separation between the contacts. When voltage was applied across the contacts during the activation energy measurement, rather than travel through the p-a-SiOx:H semiconductor the charge instead took the route of least resistance which was a very thin metal film, hence the apparent metallic behaviour.

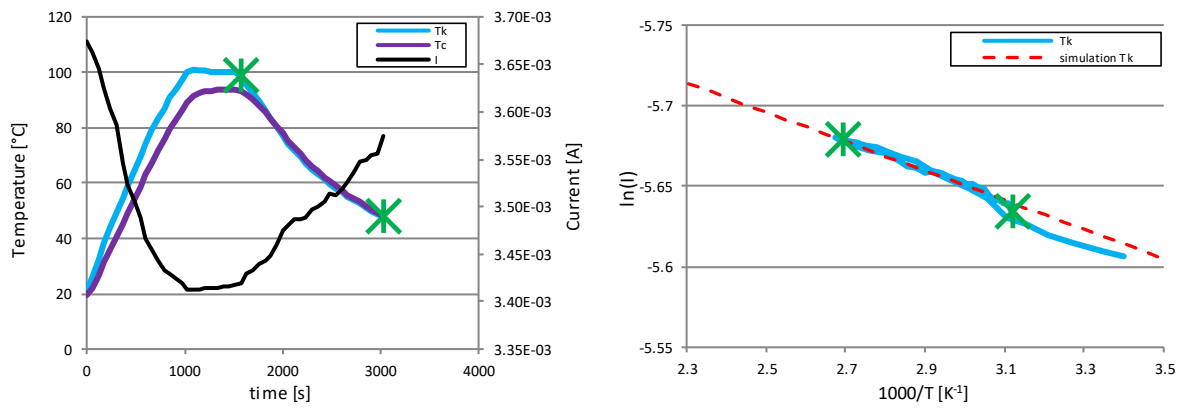


Figure 31. Activation energy measurements on sample in which the contacts were deposited via RF Magnetron sputtering. Tk is the temperature the program was set to, Tc is the actual heater temperature, I is the current. (left) The temperature dependence of the current. (right) Arrhenius plot of the temperature dependence of the current.

For the 2nd attempt of measuring the activation energy of p-a-SiOx:H, the contacts were deposited *via* thermal evaporation. Figure 32 shows the temperature dependence of the current. The line edge roughness of the contacts was much improved compared to when they were deposited via RF Magnetron Sputtering, however, now the current is in the nanoamp range and no clear relationship can be seen between current and temperature. It may be possible to suggest from the general shape of the graph that the current increases with temperature as expected with semiconductors, however, because the current alternates back and forth and the current is so low, no definite conclusion can be made. Further, because of these factors it is not possible to fit an Arrhenius plot and determine the activation energy (Figure 32, right). Because of the very low current values, Figure 32 suggests that either p-a-SiOx:H has a very low conductivity or what is being measured is noise. Without measuring the sample again on another instrument, it is not possible to know whether the former or the latter is true.

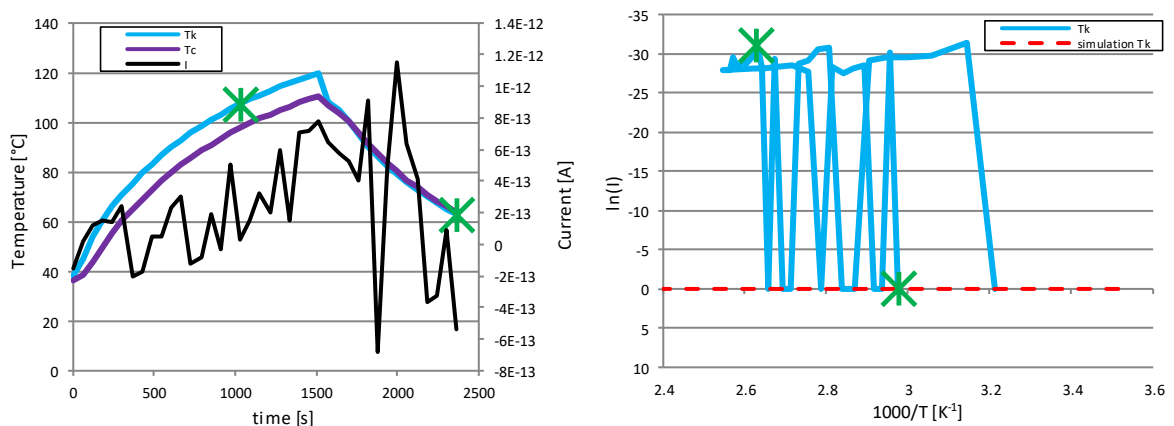


Figure 32. Activation energy measurements on sample in which the contacts were deposited via thermal evaporation. Tk is the temperature the program was set to, Tc is the actual heater temperature, I is the current. (left) The temperature dependence of the current. (right) Arrhenius plot of the temperature dependence of the current.

SOLAR CELLS

The following section describes the various different solar cell architectures tested in order to investigate the effect of using p-a-SiOx:H as a HTL in perovskite solar cells.

P-A-SiOx:H (10 & 20 nm) AS HTL

Reference Cell: Glass / ITO / NiOx NPs / Perovskite / PCBM / ZnO NP / Al

Cell Design 1: Glass / ITO / Al:ZnO / p-a-SiOx:H / Perovskite / PCBM / ZnO NP / Al

To investigate p-a-SiOx:H as a HTL, two thickness (10 and 20 nm) were employed. NiOx NPs were used as a reference HTL for comparison. Figure 33 shows pictures of the solar cells fabricated.

Note: the visible difference between the reference and p-a-SiOx:H solar cells is the way in which the cells were isolated. For the reference, small patches were wiped away whereas for the p-a-SiOx:H the entire perimeter of the cell was wiped clean of perovskite. This difference is not significant and does not affect the properties of the solar cell as both methods effectively isolate the relevant parts of the solar cell and prevent short circuiting.

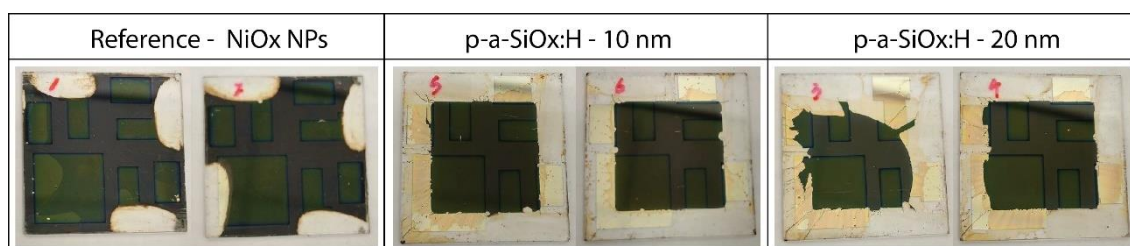


Figure 33. Pictures of the reference solar cell and the solar cells using 10 and 20 nm p-a-SiOx:H layers as the HTL.

Figure 34 shows the IV curve of the reference and Figure 36 and Figure 38 show the IV curve of the 10nm and 20 nm p-a-SiOx:H solar cells, respectively. Table 1 summarises the Jsc, Voc, FF and MPP for each cell.

Immediately obvious is the incredibly low short-circuit current of the p-a-SiOx:H solar cells, possessing short-circuit currents of 2.00 and 1.82 mA/cm² compared to 14.6 mA/cm² for the reference cell. Another noticeable thing is that the shape of the IV curves for p-a-SiOx:H also do not follow the usual “dog leg” shape which diodes exhibit, rather a straight line which is how fixed resistance materials behave. The combination of these factors leads to a very low fill factor of ~25% and a corresponding low efficiency of ~0.5%. The open circuit voltage is however normal and so these factors together suggest that there is a very high barrier to the extraction of the holes from the perovskite into the HTL.

To test whether the IV curve eventually flattens out like it should in normal solar cells, the solar cells were ramped to high negative biases (-5V). As can be seen from the reference IV curve (figure 35), the line flattens out until around -3V when it then begins to rise again. For the p-a-SiOx:H solar cells however this does not happen, instead the IV curve keeps on rising (Figure 37 and Figure 39 again indicating that there is a large extraction barrier.

#	Jsc (mA/cm ²)	Voc (mV)	FF (%)	MPP (mW/cm ²)
Reference	14.6	875	42.5	5.41
10 nm	2.00	880.9	26.05	0.46
20 nm	1.82	999	24.2	0.44

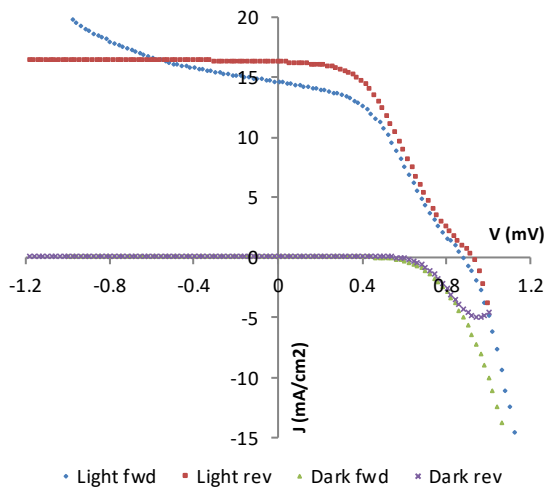


Figure 34. IV-curve of the reference cell.

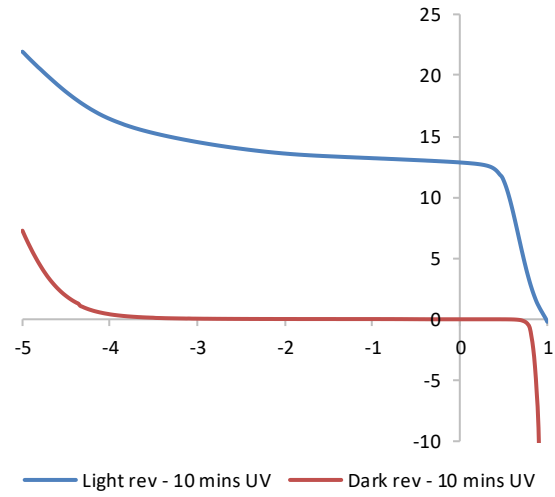


Figure 35. Reference cell reverse to -5V.

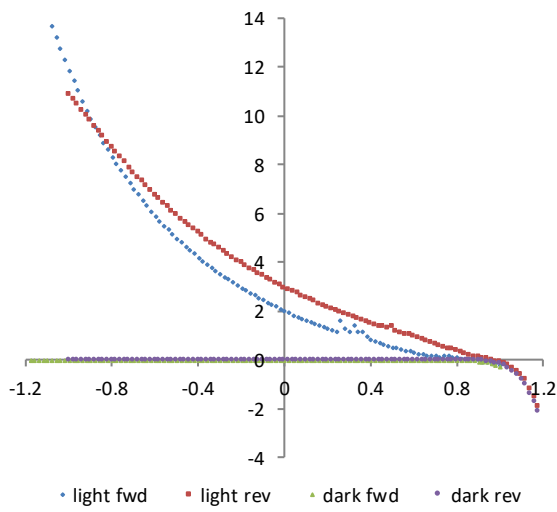


Figure 36. IV-curve of the 10 nmp-a-SiOx:HHT cell.

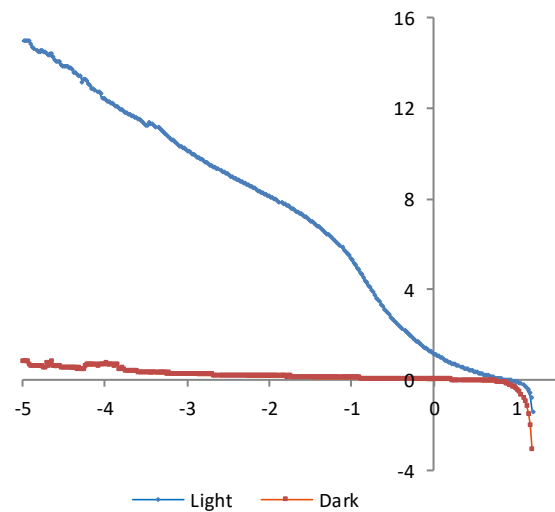


Figure 37. 10 nm p-a-SiOx:H cell reverse to -5V.

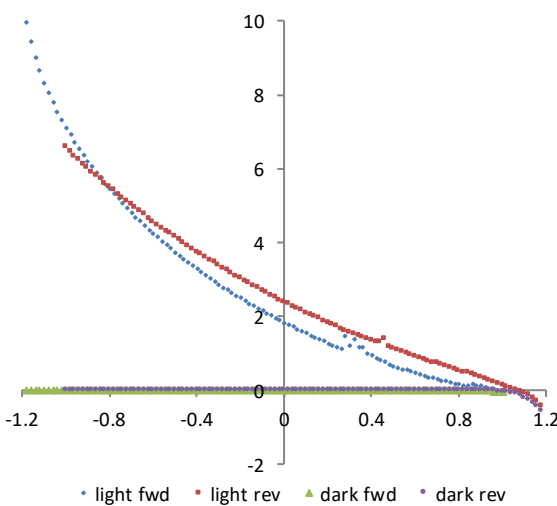


Figure 38. IV-curve of the 20 nm p-a-SiOx:H HTL cell.

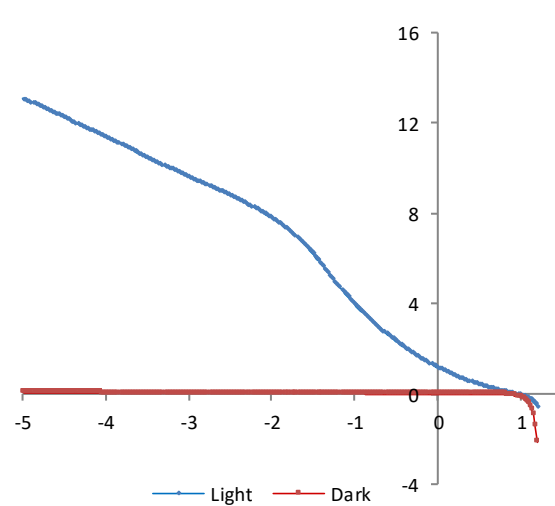


Figure 39. 20 nm p-a-SiOx:H cell reverse to -5V.

Cell Design 2: Glass / ITO / Al:ZnO / p-a-Si:H / Perovskite / PCBM / ZnO NP / Al

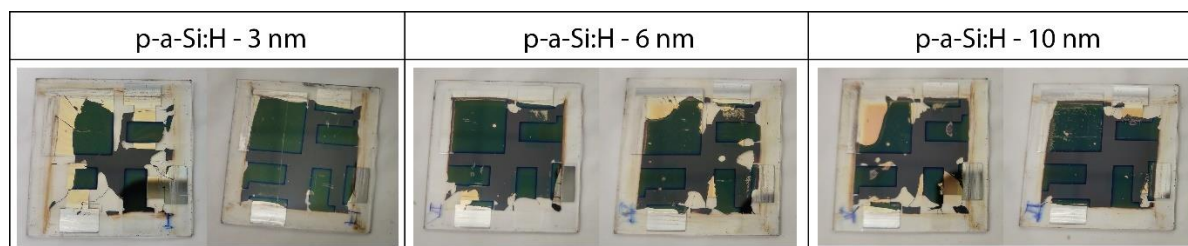


Figure 40. Pictures of the solar cells using 3, 6 and 10 nm p-a-Si:H layers as the HTL.

p-a-SiOx:H with its wide band-gap has its VB lower to the perovskite VB than p-a-Si:H, which has its VB raised relatively. Because there is more of an offset with p-a-Si:H and perovskite, there would be greater drift potential for the holes to go from the perovskite to p-a-Si:H than to p-a-SiOx:H. The downside to p-a-Si:H, and the reason why p-a-Si:H is not being currently investigated as a HTL in perovskite, is that despite there being a better VB alignment with p-a-Si:H, p-a-Si:H absorbs much more light than p-a-SiOx:H, defeating the objective of having a transparent HTL. This being said, the better band VB alignment of p-a-Si:H with perovskite would make it less likely for there to be such an extraction barrier so the short circuit current would be higher. If solar cells were fabricated with p-a-Si:H instead of p-a-SiOx:H and the short circuit current is higher, this would give some confirmation that at least part of the reason there is an extraction barrier is because of VB misalignment between p-a-SiOx:H and perovskite.

Solar cells using p-a-Si:H as HTL were fabricated and can be seen in Figure 40 and Table 2. Three different thicknesses were made, 3 nm, 6 nm, and 10 nm, in order to rule out a factor for the extraction barrier being that the p-a-SiOx:H layer was too thick. If 10 nm or 20 nm p-a-SiOx:H was really too thick to allow charge to flow through effectively, thinner layers should have a much-increased current. If, however, there is no improvement or indeed a decrease in the current then the thickness of the HTL in this size range can be ruled out.

For the 10 nm p-a-Si:H solar cell, the short-circuit current is noticeably higher than the 10 nm p-a-SiOx:H solar cell (7.3 vs. 2.0 mA/cm²), though still relatively low. Decreasing in p-a-Si:H thickness it can be seen that the current actually decreases, which eliminates the factor that the original 10 nm and 20 nm p-a-SiOx:H layers were too thick. In fact, the 3 nm p-a-Si:H layer is obviously too thin as the solar cell has broken down completely. For this cell, the HTL is so thin that it has no effect and it is as if the ITO and perovskite were brought together without a HTL. The open circuit voltage for the p-a-Si:H cells is lower than for the p-a-SiOx:H cells as is expected because p-a-Si:H possesses a smaller band gap than p-a-SiOx:H (determined from the Tauc plots, Figure 28). The shape of the p-a-Si:H IV curve shows the same linear profile as with p-a-SiOx:H, leading to an equally poor fill factor and efficiency. Despite the better VB alignment, there is clearly still an extraction barrier between the perovskite and the HTL. There must thus be another, greater, contributing factor to this than VB alignment.

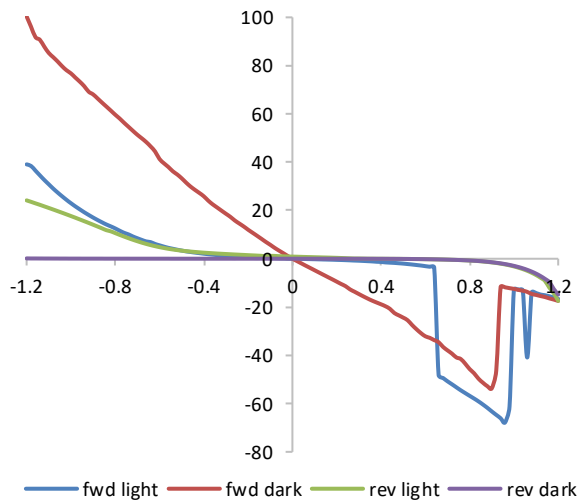


Figure 41. IV-curve of the 3 nm p-a-Si:H HTL cell.

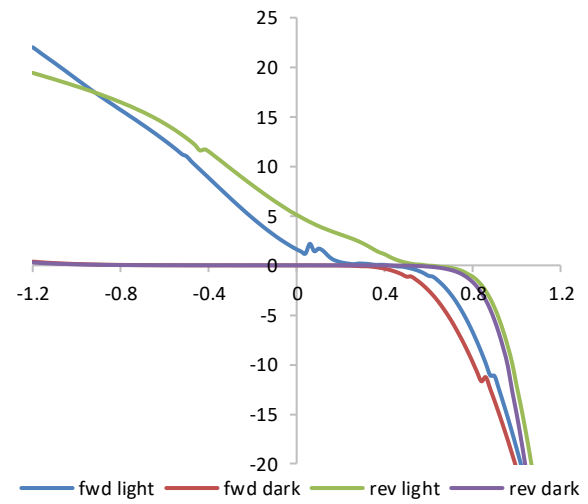


Figure 42. IV-curve of the 6 nm p-a-Si:H HTL cell.

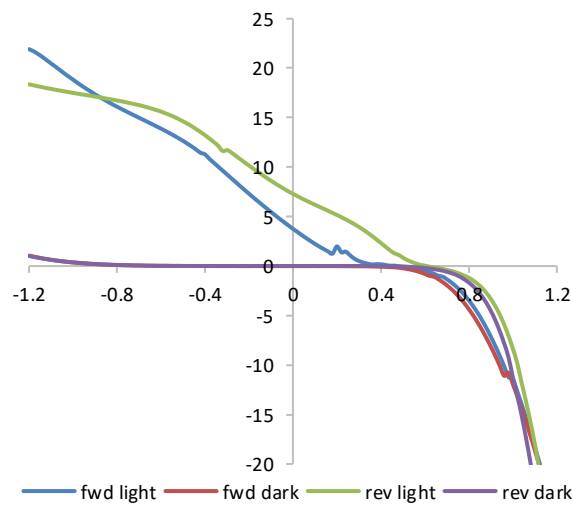


Figure 43. IV-curve of the 10 nm p-a-Si:H HTL cell.

#	Jsc (mA/cm ²)	Voc (mV)	FF (%)	MPP (mW/cm ²)
3 nm	0.38	49.6	0	0
6 nm	5.1	589	22.6	0.68
10 nm	7.3	609	26.8	1.19

WETTING ISSUE – CONTACT ANGLE MEASUREMENTS

When applying the perovskite solution onto the HTL it was noticed that the liquid did not wet the surface well. This led to the incomplete coverage of perovskite over the substrate as evident from the 20 nm p-a-SiOx:H solar cell (Figure 33) and from the majority of p-a-Si:H solar cells (Figure 40). The poor wetting could be expected because of the hydrogen termination of p-a-SiOx:H which would cause the surface to behave hydrophobically whereas the perovskite solution is hydrophilic. If the inability of the perovskite solution to wet the p-a-SiOx:H causes the inadequate coverage macroscopically, microscopically there may also be poor contact between the materials. If the perovskite only contacts the HTL in a few places, those few contact points would be the only places where the charge could conduct from one material to the other, vastly reducing the total amount of charge than can be extracted, which would explain the very low short-circuit current.

To investigate the wetting properties of the HTL it is possible to measure the contact angles liquids make with the surface and from that determine the surface energy of the solid, including the polar and dispersive components of the surface energy. It is important to understand what the polar and dispersive components of the surface energy of a solid are as these will determine how the solid will behave when liquids are introduced to it. For example, a surface which has a high polar component will interact favourably and be wet by liquids which also have a high polar component. Vice versa, the same is true for liquids and solids with largely dispersive components. Polar liquids on the other hand will not wet hydrophobic surfaces and will remain as droplets on the surface and apolar liquids will similarly not wet polar surfaces. Finding this information out could help to decide whether a different perovskite solution solvents should be used instead, or whether a specific treatment to the surface could change the components of the surface energy to better match the properties of the existing solvents.

To quantitatively determine the components of the surface energy in p-a-SiO_x:H, contact angle measurements were conducted using four test liquids and the data analysed using the Owen-Wendt method. The Owen-Wendt method is based on two fundamental equations which describe interactions between liquids and solid surfaces. The two equations are:

Young's equation:

$$\gamma_S = \gamma_{SL} + \gamma_L \cos\theta$$

and Good's equation:

$$\gamma_{SL} = \gamma_S + \gamma_L - 2(\gamma_L^D \gamma_S^D)^{\frac{1}{2}} - 2(\gamma_L^P \gamma_S^P)^{\frac{1}{2}}$$

where:

- γ_L = overall surface tension of wetting liquid,
- γ_L^D = dispersive component of liquid surface tension,
- γ_L^P = polar component of liquid surface tension,
- γ_S = overall surface energy of solid,
- γ_S^D = dispersive component of solid surface energy,
- γ_S^P = polar component of solid surface energy,
- γ_{SL} = interfacial tension between the solid and liquid,
- θ = contact angle between liquid and solid.

Combining the two equations produces:

$$\frac{\gamma_L(\cos\theta + 1)}{2(\gamma_L^D)^{1/2}} = (\gamma_S^P)^{\frac{1}{2}} \frac{(\gamma_L^P)^{1/2}}{(\gamma_L^D)^{1/2}} + (\gamma_S^D)^{\frac{1}{2}}$$

Which takes the linear form $y = mx + c$

$$y = \frac{\gamma_L(\cos\theta + 1)}{2(\gamma_L^D)^{1/2}} \quad m = (\gamma_S^P)^{1/2} \quad x = \frac{(\gamma_L^P)^{1/2}}{(\gamma_L^D)^{1/2}} \quad c = (\gamma_S^D)^{\frac{1}{2}}$$

Thus, the polar component of the surface energy can be determined by taking the square of the gradient and the dispersive component by taking the square of the intercept.

Note, in order to be able to handle the data in this way it is necessary for the polar and dispersive components of the surface tensions of the liquids to be known.

Physical properties of various liquids tested for the contact angle measurements are shown in Table 3. All of the liquids except ethylene glycol, formamide, glycerol and water, completely wet

the surface and so their contact angles could not be measured. Because EG, formamide, glycerol, and water formed droplets on the surface with measurable contact angles, these were chosen as the test liquids.

Figure 44 shows pictures of the droplets of formamide, water and ethylene glycol on the p-a-SiOx:H surface. Table 4 gives the contact angles produced when the various liquids were dropped onto p-a-SiOx:H. For comparison, the experiment was also conducted on ITO and Al:ZnO. The data was treated using the Owen-Wendt method and the graphs drawn in Figure 45.

The fitting of the data points for each of the materials was generally poor. This can be seen qualitatively by the scattered points and quantitatively by the low R^2 values. The reason for the poor fit is most likely due to deviations in the droplet size between measurements. The aim was to have 3.5 μL droplets, however, because of the viscosity of the more viscous liquids such as glycerol and ethylene glycol, it was difficult to achieve this due to there often being a delay between directing the program to dispense, the dispensing itself, and erroneous fluid flow between measurements. Furthermore, whilst for water and formamide no droplet would remain on the needle after dispensation, this was often not the case for EG and glycerol. Moreover, the volume of the droplet left on the needle would vary every time which in turn influenced the volume of the droplet dispensed onto the surface in the next measurement.

The effect of the poor fitting lead to large errors in the subsequent calculations for the surface energy and polar and dispersive components. For ITO and Al:ZnO the error in the dispersive component is actually larger than the value itself. For p-a-SiOx:H, the fitting was somewhat better than for ITO and Al:ZnO, though not good, giving smaller errors in the calculated surface energy components. Though the errors ITO and Al:ZnO are high, there is clearly a trend to be seen in which the surfaces of these materials form for the most part polar interactions with liquids and very little dispersive interactions. This can be attributed to the fact that both are metal oxides and so metal atoms could be involved in dipole-dipole, or dipole-induced dipole interactions. In addition to the aforementioned interactions, oxygen could also be involved in hydrogen bonding interactions. p-a-SiOx:H on the other hand possesses roughly equal polar and dispersive surface energy components, which is surprising as being H-terminated, dispersive interactions would be expected to dominate. Polar interactions could only form with the silicon atoms in p-a-SiOx:H suggesting that the surface is only partly H-terminated. (Note: oxygen in p-a-SiOx:H is only present as a small percentage of the composition and the oxygen atoms are found within the bulk of the material, thus not taking part in surface interactions.)

In addition to the potential increased wettability that UV + ozone may offer, the treatment would offer the added benefit of cleaning the surfaces of any contaminants which could otherwise influence their wetting behaviour. [35]

Effect of UV + Ozone treatment

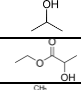
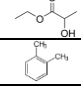
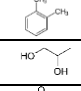
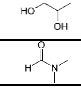
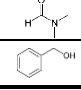
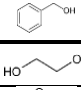
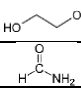
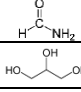
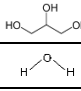
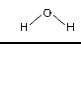
As previously mentioned, knowing the dispersive and polar components of the surface energy of p-a-SiOx:H could allow tuning of the perovskite liquids to better match the interactions they make with the surface. However, the solvent and anti-solvents used in the perovskite deposition have been already optimised for the perovskite deposition and changing them could affect the properties of the resulting perovskite layer, e.g. the homogeneity of the layer, grain size, composition, or the perovskite may not precipitate out of solution at all. This would have required a lot of experimental work which would have deviated from this reports objective.

An alternative approach was to change the surface properties of p-a-SiOx:H to better match the properties of the liquid. It has been demonstrated previously by Zhong *et al.* [36] that a UV + ozone treatment on ITO dramatically improves the wetting properties of water on its surface. In addition to the potential increased wettability, a UV + ozone treatment has the added benefit of cleaning the surfaces of any contaminants which could possibly influence wetting behaviour.

To test whether the wettability of p-a-SiOx:H could be improved, a 10 minute UV + ozone treatment was applied and the contact angles measured immediately after. For comparison the same treatment was applied to ITO and Al:ZnO. The contact angles are given in Table 45.

Remarkably, after UV + ozone treatment each material was completely wet by all of the liquids (Figure 44), giving contact angles which were close to zero (some, namely water and glycerol, were not exactly zero but the angles were very close to zero and were too acute to be detected by the software). Because no contact angles could be measured it was impossible to treat the data using the Owen-Wendt method to determine the new polar and dispersive components of the surface energy. However, qualitatively it could be seen that the UV + ozone treatment was an excellent way of improving the wettability and could be tested when fabricating new solar cells.

Table 3. Physical properties of liquids used to perform contact angle measurement on p-a-SiOx:H, ITO and Al:ZnO. The data was obtained from Ref's [32][37]

Chemical	Chemical Structure	Boiling Point, T_b (°C)	Viscosity, μ (mPa*s)	Density, ρ (g/cm ³)	Surface Tension, γ_L (mN/m)	Dispersion Component, γ_L^d (mN/m)	Polar Component, γ_L^p (mN/m)
Isopropanol		82.3	2.073	0.871	23.0		
(-)-Ethyl L-lactate		77.1	0.426	0.895	23.5	19.6	3.9
o-Xylene		144.5	0.810	0.880	30.1		
Propylene Glycol		187.6	0.581	1.036	35.4	26.4	9.0
N,N-Diethylformamide		153	0.796	0.945	37.3	32.4	4.9
Benzyl alcohol		205.2	5.474	1.042	39.0	30.3	8.7
Ethylene Glycol		197.3	16.13	1.1097	47.7	26.4	21.3
Formamide		210.5	3.302	1.1292	58.2	36.0	22.2
Glycerol		290.0	945	1.2582	63.4	37.0	26.4
Water		100.0	0.891	0.997	72.8	26.4	46.4

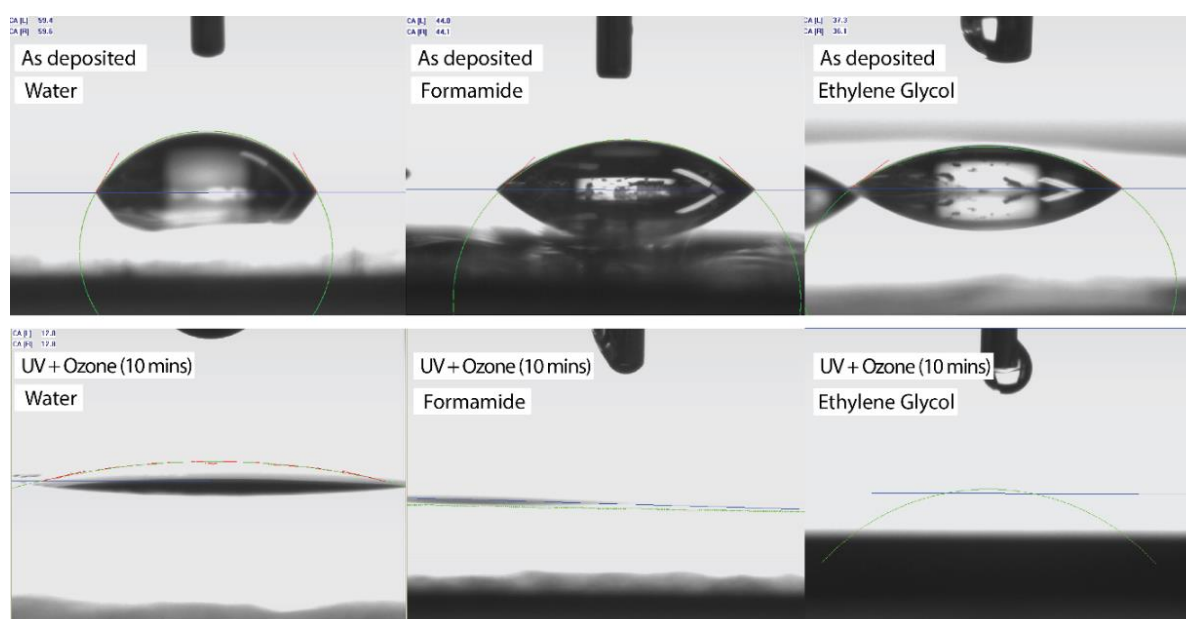
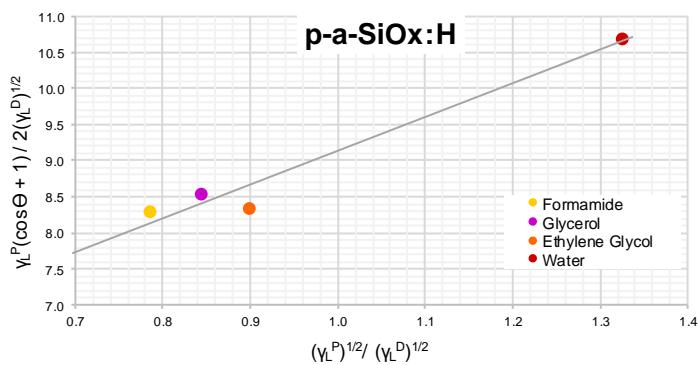


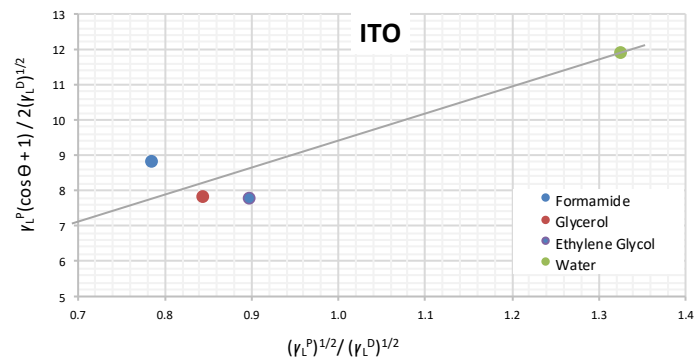
Figure 44. Pictures of the droplets of water, formamide and ethylene glycol on p-a-SiOx:H as-deposited (top) and after 10 mins UV + ozone (bottom).

Table 4. Contact angles of the liquids on the surfaces of p-a-SiOx:H, ITO and Al:ZnO as-deposited and after 10 mins UV + ozone.

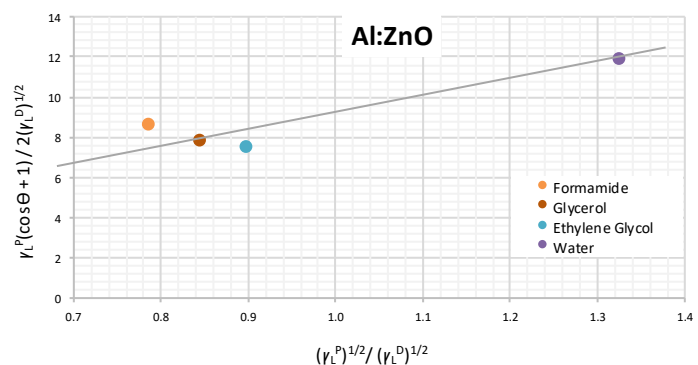
Liquid	As-deposited						UV + Ozone (10 mins)					
	p-a-SiOx:H		ITO		Al:ZnO		p-a-SiOx:H		ITO		Al:ZnO	
	θ (degrees)	std	θ (degrees)	std	θ (degrees)	std	θ (degrees)	std	θ (degrees)	std	θ (degrees)	std
Isopropanol	~0	-	~0	-	~0	-	-	-	-	-	-	-
(-)-Ethyl L-lactate	~0	-	~0	-	~0	-	-	-	-	-	-	-
O-Xylene	~0	-	~0	-	~0	-	-	-	-	-	-	-
Propylene Glycol	~0	-	~0	-	~0	-	-	-	-	-	-	-
DMF	~0	-	~0	-	~0	-	-	-	-	-	-	-
Benzyl alcohol	~0	-	~0	-	~0	-	-	-	-	-	-	-
Formamide	44.8	0.3	35.6	5.8	37.6	4.0	~0	-	~0	-	~0	-
Glycerol	50.3	1.2	60.5	2.8	59.5	5.4	~0	-	~0	-	~0	-
Ethylene Glycol	37.5	0.7	47.6	8.7	51.2	9.1	~0	-	~0	-	~0	-
Water	59.5	0.1	47.6	3.7	47.2	2.8	~0	-	~0	-	~0	-



p-a-SiOx:H		
R ²	0.93096	Error
Intercept	4.3598	0.91999
Slope	4.725	0.89342
Dispersive Component, γ_s^D	19.0	5.7
Polar Component, γ_s^P	22.3	6.0
Surface Energy of Solid (mJ/m ²)	41.3	8.2



ITO		
R ²	0.74377	Error
Intercept	2.15317	2.26779
Slope	7.16093	2.29828
Dispersive Component, γ_s^D	4.6	6.9
Polar Component, γ_s^P	51.3	23.3
Surface Energy of Solid (mJ/m ²)	55.9	24.3



Al:ZnO		
R ²	0.73861	Error
Intercept	1.91107	2.35771
Slope	7.35578	2.38941
Dispersive Component, γ_s^D	3.7	6.4
Polar Component, γ_s^P	54.1	24.9
Surface Energy of Solid (mJ/m ²)	57.8	25.7

Figure 45. Owen-Wendt graphs of the contact angles of formamide, glycerol, ethylene glycol and water on the surface of as-deposited p-a-SiOx:H, ITO and Al:ZnO. As the UV + ozone treatment led to complete wetting of the liquids on the surfaces of all materials, it was not possible to plot the Owen-Wendt graphs for them.

Reference Cell: Glass / ITO / **Cu:NiOx** / Perovskite / PCBM / ZnO NP / Al

Cell Design: Glass / ITO / **Al:ZnO** / **p-a-SiOx:H (UV + Ozone)** / Perovskite / PCBM / ZnO NP / Al

As UV + ozone treatment on p-a-SiOx:H proved to be effective at improving the wettability of liquids on its surface, a 30 mins UV + ozone treatment was applied before the addition of perovskite in a new batch of solar cells. As can be seen from Figure 46, there were no longer any wetting issues and the perovskite completely covered the HTL.

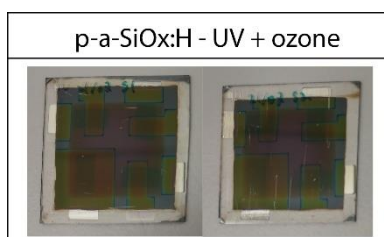


Figure 46. Picture of 20 nm p-a-SiOx:H HTL solar cells in which a 30 mins UV + ozone treatment was applied prior to the perovskite deposition.

Figure 47 shows the IV curve and Table 5 summarises the data of the UV + ozone treated solar cell. Despite improving the wettability of the perovskite on the HTL, the resulting IV curve was the worst of all p-a-SiOx:H-containing solar cells yet. Whilst the open circuit voltage was a respectable 923 mV, the incredibly low short circuit current of 0.01 mA/cm² was 100-200x less than when no UV + ozone treatment was applied, meaning that the already high hole extraction barrier had made way to one far greater and which resulted in a fill factor and efficiency of effectively zero. The reason for why this may have happened could be due to formation of a thin layer of SiO₂ (a very insulating material) on the surface as a result of the oxidation of Si by ozone.

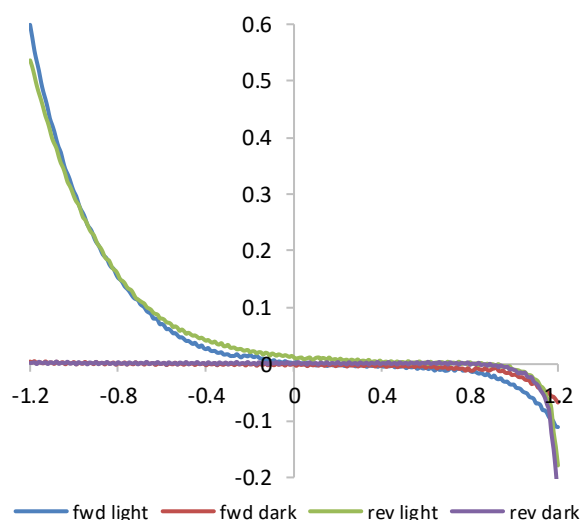


Figure 47. IV-curve of 20 nm p-a-SiOx:H HTL solar cell in which a 30 mins UV + ozone treatment was applied prior to the perovskite deposition.

#	Jsc (mA/cm ²)	Voc (mV)	FF (%)	MPP (mW/cm ²)
UV + Ozone	0.01	923	0	0

Reference Cell: Glass / ITO / Cu:NiOx / Perovskite / PCBM / ZnO NP / Al

Cell Design : Glass / ITO / Al:ZnO / p-a-SiOx:H / Cu:NiOx / Perovskite / PCBM / ZnO NP / Al

From the previous experiments it was seen that there was a high extraction barrier for the holes to go from the perovskite into the HTL. To see whether this was specific for the perovskite/HTL combination or whether this would occur with other materials into the p-a-SiOx:H as well, a compact Cu:NiOx layer was placed in between the p-a-SiOx:H and perovskite. As hole transfer between Cu:NiOx and perovskite is effective and generally HTL to HTL transfer is also effective, e.g. PTAA to NiOx, the resulting cell should perform better than for when only p-a-SiOx:H was used as the HTL.

To form the Cu:NiOx an annealing step of 290 °C for 15 minutes is required, however, the high temperature could have detrimental effects on the p-a-SiOx:H. With sufficient thermal energy Si-H bonds in the p-a-SiOx:H can be broken which in turn can allow hydrogen atoms to form gaseous molecular hydrogen. [38] The H₂ can then effuse from the material leading to the formation of microfractures which could act as defect centres for Shockley-Reid-Hall recombination, reducing the short-circuit current in the solar cell yet further. To mitigate this effect a batch of cells with a 200 °C annealing step were fabricated in addition to the usual 290 °C.

The IV curves are shown in Figure 48-51 and the data summarised in Table 6. Comparing the reference cell at 200 °C to that at 290 °C, the lower temperature is evidently insufficient to form the Cu:NiOx layer. Adding p-a-SiOx:H then diminishes the performance further to that of noise, though another explanation for the noise-like IV curve could be a poor electrical contact between the solar cell electrodes and the MiniSunSim IV instrument.

The reference at 290 °C shows clearly better performance than at 200 °C, however, the IV characteristics are still quite bad, with the IV curve following a straight line from the V_{oc} to the I_{sc}, giving a low FF and efficiency of only 1.73%. Inserting p-a-SiOx:H in between the ITO and Cu:NiOx, however, then kills the current completely even though the hole transfer is between HTLs. Though the Cu:NiOx solution wet the p-a-SiOx:H better than when the perovskite is applied directly, it is not known what the interface looks like on the microscopic scale. It could be that, as is suspected to be the cause when p-a-SiOx:H is used solely as the HTL, that there is not a good contact between the Cu:NiOx and p-a-SiOx:H, limiting the amount of charge that can be extracted and giving a low short-circuit current. Without further analysis of the interface on the microscopic scale, for instance, with an FIB-SEM, firm conclusions cannot be drawn.

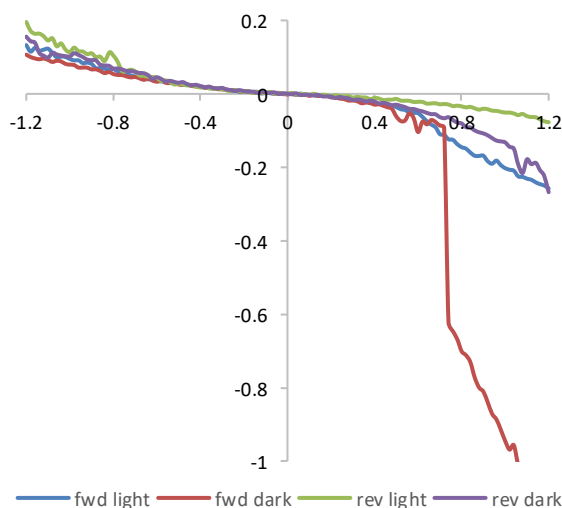


Figure 48. IV-curve of reference cell annealed at 200 °C.

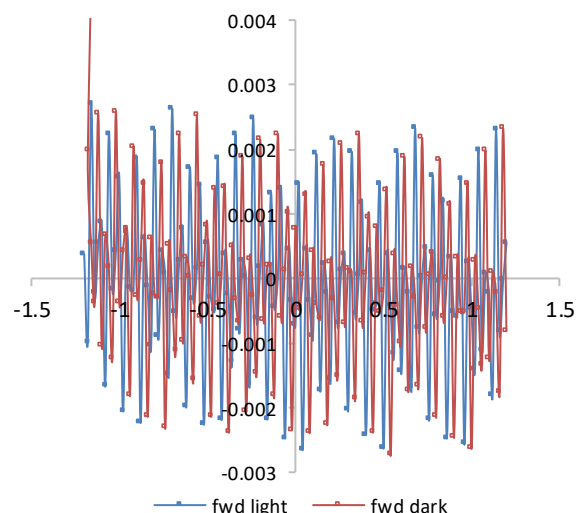


Figure 49. IV-curve of p-a-SiOx:H + Cu:NiOx HTL cell annealed at 200 °C.

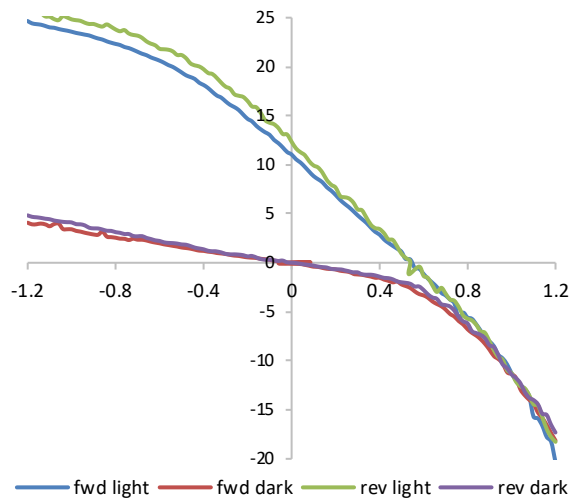


Figure 50. IV-curve of reference cell annealed at 290°C.

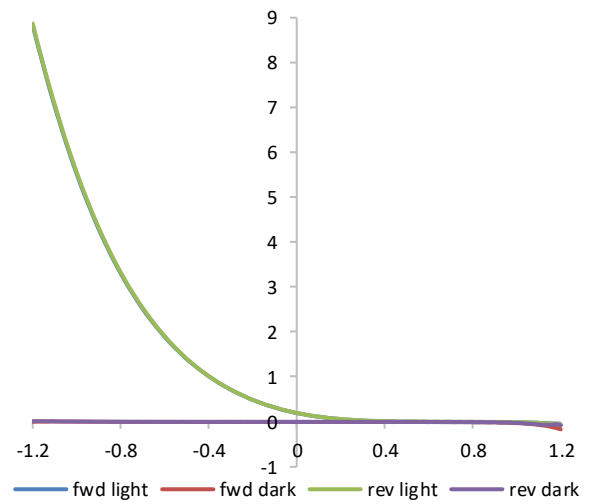


Figure 51. IV-curve of p-a-SiOx:H + Cu: NiOx HTL cell annealed at 290 °C

Table 6. IV parameters of reference cells and p-a-SiOx:H + Cu: NiOx HTL cells annealed at 200 and 290 °C					
	#	Jsc (mA/cm ²)	Voc (mV)	FF (%)	MPP (mW/cm ²)
Anneal 200 °C	Reference	0.005	-8.8	0	0
	Cell	-	-	-	-
Anneal 290 °C	Reference	12.3	548	25.6	1.73
	Cell	0.20	916	5.5	0.01

7. CONCLUSION & FUTURE WORK

In all instances of p-a-SiOx:H being used as a HTL in the solar cells fabricated in this report, there was a detrimental effect on the solar cell performance compared to solar cells using other HTLs, *i.e.* NiOx NPs and Cu:NiOx. The effect on the IV characteristics of the cells was a great reduction in the short-circuit current and a loss in the fill factor arising from the curve being linear. Whilst the open circuit voltage was good, the low short-circuit current and fill factor resulted in very low efficiency cells – the hero cell was only 0.46 % when a 10 nm layer of p-a-SiOx:H was used exclusively as the HTL, whilst the worst cells gave effectively 0 % efficiency, e.g. with UV + ozone treatment, and when Cu:NiOx and p-a-SiOx:H were used in combination.

The reason for the poor performance of the cells appears to be because of a large barrier to the extraction of the holes into the p-a-SiOx:H, whether this be from the perovskite directly or from other materials such as the Cu:NiOx. The cause of the barrier seems to be likely due to a poor contact between the p-a-SiOx:H and the other materials, which may arise because of poor wetting. Poor contact between the materials would lead to few contact points through which the charge be extracted.

However, what cannot be ruled out is that p-a-SiOx:H (at least the material fabricated in this report) may simply not be very conductive to holes. The inability to measure the activation energy due to the current being so low as to be indistinguishable from noise, suggests that p-a-SiOx:H does have a very low conductivity. The mobility of charges in perovskite is known to be incredibly high. If the electrons, once separated from the holes travel all the way through the perovskite layer, are efficiently extracted by the ETL and cathode, travel all the way around the circuit and are injected into the anode or HTL, then the holes and electrons will recombine and the current will be very low. Normally, if recombination occurs at the HTL/absorber interface a corresponding drop in the open-circuit voltage will be observed, however, if the recombination happens in the anode or HTL there will not be this drop. This may be a possibility in this report which would not be noticed from simply looking at the IV-curve.

Another contributing factor could be a non-optimum band alignment between the valence band of the p-a-SiOx:H and the valence band of the perovskite or Cu:NiOx. The determination of the work function from the Kelvin probe measurements yielded a work function somewhat lower than was expected. The effect of this when bringing the HTL and perovskite together would be that the VB of the HTL (and ETL) would not be raised as it would be if the HTL had a higher work function. This would create less of an electric field to drive the hole drift current from the absorber layer to the HTL. In the most extreme circumstance of the work function of the HTL being even lower, or if the work function of perovskite was higher, an electric field in the opposite direction could be created. This would have a repulsive effect for the holes and would drive them away from the HTL. As discussed in the “Characterisation of p-a-SiOx:H” section, there is some uncertainty as to the precise value of the workfunction of the p-a-SiOx:H. Furthermore, the work function of the triple-cation perovskite was not measured directly, rather a literature value was used. If the actual work function of each of these materials deviates significantly from what they are thought to be, it could be the case that a negative electric field is created when the two materials are brought together. Considering the very low short-current of the fabricated solar cells this may be a possibility.

Future Work

Further work can be done to investigate the potential reasons for the poor cell performance. To see whether the contact between the perovskite and p-a-SiOx:H is good, microscopic techniques such as FIB-SEM could be used to image the interface. This technique enables a 3D cross-sectional image of the interface to be gained which would allow the opportunity to visually see whether the

two materials contact each other well or whether there are gaps and voids present. A different approach would be to avoid the possibility of wetting issues arising from the solution processing the perovskite, by vapour depositing the p-a-SiO_x:H onto the perovskite directly, or alternatively, vapour deposit the perovskite onto the p-a-SiO_x:H. To investigate the conductivity of the p-a-SiO_x:H, new more precise measurements should be taken. This is because it is not sure whether the p-a-SiO_x:H was indeed so insulating that there was so little current it was blocked out by noise, or whether the instrument was not working properly. If it turns out that the p-a-SiO_x:H has a very low conductivity, the composition could be tuned to improve this, e.g. increasing the p-type doping. Composition control can also be employed to tune the band-gap and increase the work function so that the band-alignment can be optimised. In conjunction, other characterisation techniques could be used to possibly gain more precise measurements of the band-gap and work function. Using multiple characterisation techniques would enable comparison with the values measured in this report and check their validity. To get a more accurate band-gap value, ellipsometry should be used to determine the absorption coefficient as determining the absorption coefficient from the transmission spectra ignores any reflection/scattering of light on the materials surface, introducing error into the calculation. For a more precise work function measurement, ultraviolet photoelectron spectroscopy (UPS) should be used.

Can p-a-SiO_x:H be used as a HTL in PSC's?

From the experiments conducted in this report it would seem that p-a-SiO_x:H cannot be used as a HTL in perovskite solar cells, at least not yet. If the points noted are investigated thoroughly a clearer, more definite view can be reached of its feasibility as a potential, viable HTL candidate. Further research is required.

8. ACKNOWLEDGEMENTS

The nearly six months I have spent at Solliance ECN has given me a very good insight into the world of photovoltaics – a subject which I have subsequently developed a passion for. One of the things I loved about the research at Solliance, and the organisation itself, was the applied nature of the research and the goal of trying to improve Perovskite solar cells for real world application and future commercialisation. The idea that the small contribution I made may one day be used in perovskite solar panels that you find on your roof at home, was really a motivation.

I am really grateful for the opportunity to have done this internship at Solliance ECN, however, I likely would never have thought about going down the photovoltaics route had it not been for the Solar Energy Physics course I took Utrecht University, taught by dr. Wilfried van Sark. Almost immediately when I started the course I developed a strong interest in the subject and urge to learn as much about it as possible. The lectures were well taught, we had a day trip to ECN in Petten and there were some excellent guest lectures by invited speakers. It seemed then only natural that when I was to do an internship at Solliance ECN for me to ask Wilfried to be my supervisor from Utrecht University. With this I would like to thank him for all his contributions and guidance during the Solar Energy Physics course and during my internship.

At Solliance my two supervisors were dr. Sjoerd Veenstra (main) and dr. Dong Zhang (daily). I would like to thank them both for their guidance throughout the internship, both with regards to my research and otherwise.

My internship was very collaborative and the research I did would not have been possible without the help of various individuals. A special mention therefore goes to Maarten Dörenkämper for his assistance in performing depositions with the PECVD and to Klaas Bakker for his help with various equipment in the lab and fixing them when they broke.

Lastly, I would like to thank all the interns in ECN, TNO and SEAC for the many interesting discussions and collaborations. A special mention goes to the Dutch guys Rick Verhage, Jeroen de Cloet, Aron van Damme, and Guillaume Croes as well as the French guys Fabian Mangeonjean, Maxime Broit, Clement Guerin, and Christophe Bonneau, for making lunchtimes very enjoyable. Finally, thanks to all the others who made played beach volleyball possible - a sport which I had not really played before but which now I really love.

9. APPENDICES

APPENDIX A – WORK FUNCTIONS OF VARIOUS MATERIALS MEASURED USING THE KELVIN PROBE

Various materials other than p-a-SiOx:H and p-a-Si:H had their work function measured using the Kelvin Probe, these are given in the table below.

Kelvin Probe Measurements			
Material		WF (eV)	std
c-Si wafer	As-received	4.59	0.08
p-a-Si:H	As-deposited	4.51	0.07
p-a-SiOx:H	As-deposited	4.80	0.09
ITO	As-deposited	5.02	0.10
	20 mins UV + Ozone	5.46	0.09
	30 mins UV + Ozone	5.46	0.07
IO:H	As-deposited	4.94	0.08
	30 mins UV + Ozone	5.34	0.08
CuGaOx	As-deposited	4.94	0.09
CuSCN	As-deposited	5.38	0.09
CuO	As-deposited	4.95	0.07
	30 mins UV	4.95	0.07
CuI	As-deposited	5.23	0.08
	30 mins UV	4.60	0.07
NiO	As-deposited	5.40	0.10
	30 mins UV	5.22	0.08

APPENDIX B – PROPERTIES OF ITO

Hall probe measurements were conducted on ITO layers of various thicknesses, the properties of these layers are given below.

Thickness (nm)	Sheet resistance (Ω/sq)	Resistivity ($\Omega \text{ cm}$)	Carrier density, n (cm^{-3})	Mobility, μ ($\text{cm}^2 \text{ V}^{-1} \text{ s}^{-1}$)	E_g (eV)
109	37	3.9×10^{-4}	3.3×10^{20}	49	3.79
140	17	2.3×10^{-4}	5.6×10^{20}	49	3.79
240	15	3.5×10^{-4}	3.5×10^{20}	51	3.79
323	16	5.0×10^{-4}	2.7×10^{20}	47	3.79

10. REFERENCES

- [1] A. Louw, 'Clean Energy Investment Trends, 2Q 2017', 2017.
- [2] IRENA, 'Solar PV module cost learning curve for crystalline silicon and thin-film', *International Renewable Energy Agency*, 2015. [Online]. Available: <http://costing.irena.org/charts/solar-photovoltaic.aspx>. [Accessed: 12-Aug-2017].
- [3] M. Jacoby, 'The future of low-cost solar cells', *Chem. Eng. News*, vol. 94, no. 18, pp. 30–35, 2016.
- [4] J. Libal and R. Kopacek, 'Limit for industrial c-Si solar cells reached in 2030: what next?', *PV-Tech*, 2015. [Online]. Available: https://www.pv-tech.org/guest-blog/limit_for_industrial_c_si_solar_cells_reached_in_2030_what_next. [Accessed: 10-Aug-2017].
- [5] T. He *et al.*, 'Superconductivity in the non-oxide', vol. 411, no. May, pp. 6–8, 2001.
- [6] Y. Moritomo, a. Asamitsu, H. Kuwahara, and Y. Tokura, 'Giant magnetoresistance of manganese oxides with a layered perovskite structure', *Nature*, vol. 380, no. 6570, pp. 141–144, 1996.
- [7] N. Labhasetwar *et al.*, 'Perovskite-type catalytic materials for environmental applications', *Sci. Technol. Adv. Mater.*, vol. 16, no. 3, p. 36002, 2015.
- [8] M. A. Green, A. Ho-Baillie, and H. J. Snaith, 'The emergence of perovskite solar cells', *Nat. Photonics*, vol. 8, no. 7, pp. 506–514, 2014.
- [9] W. Hicks, 'Claims for solar cell efficiency put to test at NREL', 2016. [Online]. Available: <https://phys.org/news/2016-02-solar-cell-efficiency-nrel.html>. [Accessed: 12-Aug-2017].
- [10] M. Maehlum, 'The Real Lifespan of Solar Panels', *Energy Informative*, 2014. [Online]. Available: <http://energyinformative.org/lifespan-solar-panels/>. [Accessed: 11-Aug-2017].
- [11] G. Grancini *et al.*, 'One-Year stable perovskite solar cells by 2D/3D interface engineering.', *Nat. Commun.*, vol. 8, p. 15684, 2017.
- [12] B. Conings *et al.*, 'Intrinsic Thermal Instability of Methylammonium Lead Trihalide Perovskite', *Adv. Energy Mater.*, vol. 5, no. 15, pp. 1–8, 2015.
- [13] P. Docampo, J. M. Ball, M. Darwich, G. E. Eperon, and H. J. Snaith, 'Efficient organometal trihalide perovskite planar-heterojunction solar cells on flexible polymer substrates.', *Nat. Commun.*, vol. 4, p. 2761, 2013.
- [14] H.-S. Kim *et al.*, 'Lead iodide perovskite sensitized all-solid-state submicron thin film mesoscopic solar cell with efficiency exceeding 9%.', *Sci. Rep.*, vol. 2, no. 7436, p. 591, 2012.
- [15] N. Yaghoobi Nia, F. Matteocci, L. Cina, and A. Di Carlo, 'High Efficiency Perovskite Solar Cell Based on Poly (3-hexylthiophene) (P3HT): The Influence of P3HT Molecular Weight and Mesoscopic Scaffold Layer', *ChemSusChem*, p. In press, 2017.
- [16] J. H. Heo *et al.*, 'Efficient inorganic-organic hybrid heterojunction solar cells containing perovskite compound and polymeric hole conductors', *Nat Phot.*, vol. 7, no. 6, pp. 486–491, 2013.
- [17] J. A. Christians, R. C. M. Fung, and P. V. Kamat, 'An Inorganic Hole Conductor for Organo-Lead Halide Perovskite Solar Cells. Improved Hole Conductivity with Copper Iodide', *J. Am.*

- Chem. Soc.*, vol. 136, no. 2, pp. 758–764, 2014.
- [18] P. Qin *et al.*, ‘Inorganic hole conductor-based lead halide perovskite solar cells with 12.4% conversion efficiency’, *Nat. Commun.*, vol. 5, no. May, pp. 1–6, 2014.
- [19] C. C. Stoumpos and M. G. Kanatzidis, ‘The Renaissance of Halide Perovskites and Their Evolution as Emerging Semiconductors’, *Acc. Chem. Res.*, vol. 48, no. 10, pp. 2791–2802, 2015.
- [20] Z. Song, S. C. Watthage, A. B. Phillips, and M. J. Heben, ‘Pathways toward high-performance perovskite solar cells: review of recent advances in organo-metal halide perovskites for photovoltaic applications’, *J. Photonics Energy*, vol. 6, no. 2, p. 22001, 2016.
- [21] G. Xing *et al.*, ‘Low-temperature solution-processed wavelength-tunable perovskites for lasing’, *Nat. Mater.*, vol. 13, no. 5, pp. 476–80, 2014.
- [22] Y. Sun, J. Peng, Y. Chen, Y. Yao, and Z. Liang, ‘Triple-cation mixed-halide perovskites: towards efficient, annealing-free and air-stable solar cells enabled by Pb(SCN)₂ additive’, *Sci. Rep.*, vol. 7, no. April, p. 46193, 2017.
- [23] EPFL, ‘Perovskite Cells for Tandem Applications’, 2016. [Online]. Available: <http://pvlab.epfl.ch/page-124775-en.html>. [Accessed: 28-Jul-2017].
- [24] C. Zhang *et al.*, ‘Optical and Electrical Effects of p-type $\mu\text{-SiO}_x\text{:H}$ in Thin-Film Silicon Solar Cells on Various Front Textures’, *Int. J. Photoenergy*, vol. 2014, pp. 1–10, 2014.
- [25] S. Swann, ‘Magnetron sputtering’, *Phys. Technol.*, vol. 19, no. 6, pp. 67–75, 1988.
- [26] X. Zhang, B. Demarex, and S. De Wolf, ‘Sputtered Hydrogenated Amorphous Silicon for Silicon Heterojunction Solar Cell Fabrication’, *Energy Procedia*, vol. 55, pp. 865–872, 2014.
- [27] R. Bosco, J. Van Den Beucken, S. Leeuwenburgh, and J. Jansen, ‘Surface Engineering for Bone Implants: A Trend from Passive to Active Surfaces’, *Coatings*, vol. 2, no. 3, pp. 95–119, 2012.
- [28] A. Cremona, E. Vassallo, A. Merlo, A. Srikantha Phani, and L. Laguardia, ‘Synthesis by plasma-enhanced chemical-vapor deposition and characterization of siliconlike films with hydrophobic functionalities for improved long-term geometric stability of fiber-reinforced polymers’, *J. Mater. Res.*, vol. 23, no. 4, pp. 1042–1050, 2008.
- [29] D. Meyerhofer, L. E. Scriven, and L. E. Scriven, ‘Characteristics of resist films produced by spinning’, *J. Appl. Phys.*, vol. 49, no. 7, pp. 3993–3997, Jul. 1978.
- [30] A. Kahn, ‘Fermi level, work function and vacuum level’, *Mater. Horiz.*, vol. 3, no. 1, pp. 7–10, 2016.
- [31] HyperPhysics, ‘Hall Effect’. [Online]. Available: <http://hyperphysics.phy-astr.gsu.edu/hbase/magnetic/Hall.html>. [Accessed: 18-Jul-2017].
- [32] C. Rulison, ‘Models for Surface Energy Calculation’, *Krus. USA Tech. Note 306*, pp. 1–8, 1999.
- [33] ‘Work Functions for Photoelectric Effect’, *HyperPhysics*, 2016. [Online]. Available: <http://hyperphysics.phy-astr.gsu.edu/hbase/Tables/photoelec.html>. [Accessed: 23-Aug-2017].
- [34] M. Trijssenaar, ‘Hydrogenated amorphous silicon and p/i-heterojunctions’, Technical University Delft, 1995.
- [35] A. Moldovan *et al.*, ‘Simple cleaning and conditioning of silicon surfaces with UV/ozone Sources’, *Energy Procedia*, vol. 55, pp. 834–844, 2014.

- [36] Z. Zhong, Y. Zhong, C. Liu, S. Yin, W. Zhang, and D. Shi, 'Study on the surface wetting properties of treated indium-tin-oxide anodes for polymer electroluminescence devices', *Phys. Status Solidi Appl. Res.*, vol. 198, no. 1, pp. 197–203, 2003.
- [37] 'Physical Properties of Liquids', *TriMen Chemicals*, 2016. [Online]. Available: http://www.trimen.pl/witek/ciecze/old_liquids.html. [Accessed: 17-Aug-2017].
- [38] S. De Wolf and M. Kondo, 'Nature of doped a-Si:H/c-Si interface recombination', *J. Appl. Phys.*, vol. 105, no. 10, pp. 1–7, 2009.